Ensemble numerical simulation of permafrost over the Tibetan Plateau from Flexible Permafrost Model: 1950–2023

Wen Sun and Bin Cao

State Key Laboratory of Tibetan Plateau Earth System Environment and Resources (TPESER), National Tibetan Plateau Data Center (TPDC), Institute of Tibetan Plateau Research, Chinese Academy of Sciences, Beijing, China

Correspondence: Bin Cao (bin.cao@itpcas.ac.cn)

Abstract. Permafrost is a subsurface phenomenon that is difficult to be measured directly, and understanding its dynamics as well as influences under a warming climate depends critically on numerical simulations. However, this task presents significant challenges as the state-of-the-art land surface models are weak in their ability to represent permafrost processes. In this study, we introduce a new land surface scheme specifically designed for permafrost applications, the Flexible Permafrost Model (FPM). This model serves as an adaptable framework for implementing innovative parameterizations of permafrost-related physics. The FPM accounts for heat flow at and below the soil surface, while simultaneously resolving the land-atmosphere energy exchanges through comprehensive treatment of radiative balance and turbulent flux dynamics. We simulate the ground thermal regime and test the model with a network of permafrost measurements across the Tibetan Plateau.

Our result yields root mean square error values of 1.1 m for the thickness of the active layer and 1.3 $^{\circ}\mathrm{C}$ for the mean annual ground temperature of permafrost. We estimate that the current extent of permafrost (2010–2023) on the Tibetan Plateau is approximately $1.18 \pm 0.02 \times 10^6$ km^2, which aligns closely with published estimates. Long-term simulations indicate that the permafrost temperature has increased by 0.28 $^{\circ}\mathrm{C}$ since 1980 with a decreased area of 13.8×10^4 km^2 ($\sim$10.8 $\%$). These ensemble simulations provide valuable information on the dynamics of permafrost over the Tibetan Plateau. Furthermore, our findings suggest that current land surface models, which utilize shallow soil columns (typically $\sim$3 m), are insufficient for permafrost simulations over the Tibetan Plateau due to the typically deep active layer (that is, 2.79 ± 0.86 m by mean) and may not be suitable for future projections.

1 Introduction

Permafrost regions occupy more than one-fifth of the exposed land area in the Northern Hemisphere (Gruber, 2012). Long-term records revealed steady warming of permafrost over the past several decades at a global scale (Biskaborn et al., 2019). This has led to significant degradation of the permafrost, such as a deepening active layer (Cao et al., 2018; Biskaborn et al., 2019), decreased permafrost area (Chadburn et al., 2017; Sun et al., 2022; Langer et al., 2024), expanded thermokarst (Wellman et al., 2013; Chen et al., 2021), and potential carbon decomposition (Schuur et al., 2015). Permafrost degradation has considerable influences on ecosystems, hydrological systems, and the integrity of the infrastructure (Hjort et al., 2018; Walvoord et al.,

2019; Schuur and Mack, 2018). Therefore, detailed investigations of changes in permafrost in response to a warming climate are crucial for sustainable management and adaptation strategies.

Despite permafrost's importance, direct permafrost measurements, such as borehole temperature, are rare due to harsh environments and high costs (Biskaborn et al., 2015). This is especially true on the Tibetan Plateau (TP), where complex terrain and high altitudes impose further constraints on permafrost research (Cao et al., 2017b, 2019b). For these reasons, there is often a lack of essential *in situ* information to develop suitable statistical models (Zhao et al., 2021; Cao et al., 2021). Therefore, process-based simulation is an increasingly important tool for transient assessment of permafrost conditions and dynamics.

The TP, also known as the Third Pole, has the largest extent of permafrost in the low-middle latitudes (Cao et al., 2019b). Significant efforts have been made to understand the permafrost changes over the TP based on simulations. A large portion of these contributions comes from the hydrological community, employing models originally designed to simulate hydrological processes in permafrost-affected regions. Many of the models implemented detailed representations of hydrological processes (e.g., water mass balance) while simplifying the surface energy balance and soil thermal processes. For instance, the DHTC model parameterized ground heat conduction as a linear function of net radiation (Linmao et al., 2024), and the FLEXTopo-FS model uses the empirical method (i.e., Stefan equation) for freeze/thaw processes (Gao et al., 2022). In addition to such hydrological models, the process-based models used for recent transient permafrost simulation over the TP can be generally divided into geothermal numerical models (i.e., GIPL model) and the common land surface models (i.e., CLM and Noah-MP). The geothermal numerical models typically have rich permafrost-specific processes, such as suitable numerical solver in heat transfer with soil phase changes (Nicolsky et al., 2007; Tubini et al., 2021), deep soil column (tens to hundreds of meters), and well-defined lower boundary, but lack representation of land-atmosphere interactions (i.e., Qin et al., 2017; Sun et al., 2023). On the other hand, the land surface models benefits from the consideration of land-atmosphere processes, and therefore outperform in describing the responses of permafrost to climate warming (i.e., Guo et al., 2018; Wu et al., 2018; Zhang et al., 2021; Cao et al., 2022).

Recently, a few permafrost-specific land surface scheme models–combining the advantages of these two types of models–were proposed. The stand-alone models yield promising potential for application to cross-scale permafrost processes (Fiddes et al., 2015; Westermann et al., 2016). However, dedicated stand-alone permafrost models remain scarce for the TP. Most existing simulations rely on distributed hydrological models that have been enhanced with permafrost process representations (e.g., Gao et al., 2018; Song et al., 2020). Although these models generally offer more realistic and detailed simulations of permafrost-influenced hydrological processes, they are typically confined to site or regional scales and short time periods due to their demand for extensive spatial data and high computational cost (i.e., Pan et al., 2016; Zhang et al., 2017; Zheng et al., 2020).

In this study, we introduce a new land surface scheme specifically designed for permafrost applications, the Flexible Permafrost Model (FPM). This model serves as a flexible platform for a variety of permafrost processes. The suitability of the new model was carefully evaluated, we then employed it in analyzing the long-term (1950–2023) permafrost thermal regime over the TP based on the ensemble simulation. Specifically, this study

1. gives a detailed description of the model conceptualization, structure, and key parameterizations;

2. evaluates the model performance in reproducing permafrost characteristics based on the ensemble approach, such as active layer thickness (ALT), and the thermal state;

3. interprets current conditions and historical changes of permafrost in response to climate change from the stand-alone simulations;

4. proposes insights for future model developments.

2 Flexible Permafrost Model (FPM)

The FPM is land-surface scheme designed, so that algorithms and process parameterizations can easily be transferred, and the ensemble simulation could be produced based on specific scientific objectives. FPM accounts for heat flow with phase change at and below the soil surface, while also describing the energy exchange with the atmosphere by considering radiative and turbulent fluxes. In this study, we give the detailed introduction and evaluation of FPM and employed it in analyzing large-scale permafrost studies. The nomenclature and key model parameters are given in Table 1, and constants are in Table E1.

2.1 Surface energy balance

The ground or snow surface temperature ($\mathrm{T_{S0}}$, K) was treated as upper boundary of the soil column. To derive $\mathrm{T_{S0}}$, a physically-based surface energy balance scheme for different land surface cover types was coupled to FPM, and was formulated as:

$$(1-\alpha)\,Q_{si} + Q_{li} + Q_{le} + Q_h + Q_e = Q_c \tag{1}$$

where $\mathrm{Q_{si}}$ is the incoming shortwave radiation, $\mathrm{Q_{li}}$ is the incoming longwave radiation, $\mathrm{Q_{le}}$ is the emitted longwave radiation, $\mathrm{Q_h}$ is the turbulent exchange of sensible heat, $\mathrm{Q_e}$ is the turbulent exchange of latent heat, and $\mathrm{Q_c}$ is the energy transport due to conduction. All the above energy terms have units of $\mathrm{W\,m^{-2}}$. The α $(-)$ is the surface albedo, obtained as a fraction-weighted average of albedo from snow-free (α_{g}) and snow-covered (α_{sn}) areas.

$$\alpha = (1-SCF)\cdot\alpha_g + SCF\cdot\alpha_{sn} \tag{2}$$

where SCF $(-)$ is the snow cover fraction (see Sec. 2.2), and α_{g} is from MODIS products whenever snow is not present (Table 2).

The $\mathrm{Q_{si}}$ and $\mathrm{Q_{li}}$ are either from observations or from a reanalysis dataset (Table 2). The $\mathrm{Q_{le}}$ is computed under the assumption that ground (snow) emits as a gray body:

$$Q_{le} = -\varepsilon_s \sigma {T_{s0}}^4 \tag{3}$$

where ε_{s} $(-)$ is the surface emissivity, and σ is the Stefan-Boltzmann constant of $5.67\times10^{-8}\ \mathrm{W\,m^{-2}\,K^{-4}}$. The ε_{s} was set to 0.92 for ground surface, and 0.98 for snow surface (Fleagle and Businger, 1981).

Table 1. Nomenclature and input parameters for Flexible Permafrost Model (FPM).

Symbol	Parameter	Value or range	Unit
C	apparent heat capacity		$\mathrm{J\,m^{-3}\,K^{-1}}$
CV	volumetric heat capacity		$\mathrm{J\,m^{-3}\,K^{-1}}$
L	volumetric latent heat of fusion for ice		$\mathrm{J\,m^{-3}}$
θ_u	volume contents of unfrozen water		$\mathrm{m^3\,m^{-3}}$
θ_i	volume contents of ice		$\mathrm{m^3\,m^{-3}}$
θ_a	volume contents of air		$\mathrm{m^3\,m^{-3}}$
θ_R	soil moisture in root zone		$\mathrm{m^3\,m^{-3}}$
θ_v	soil moisture in vadose zone		$\mathrm{m^3\,m^{-3}}$
θ_{sat}	saturated soil moisture		$\mathrm{m^3\,m^{-3}}$
θ_r	residual soil moisture		$\mathrm{m^3\,m^{-3}}$
θ_{fc}	soil field capacity		$\mathrm{m^3\,m^{-3}}$
ϕ	soil porosity		$\mathrm{m^3\,m^{-3}}$
α	surface albedo		Dimensionless
α_g	snow-free surface albedo		Dimensionless
α_{sn}	snow albedo	0.50–0.85	Dimensionless
α_{sn}^{max}	maximum snow albedo	0.85	Dimensionless
α_{sn}^{min}	minimum snow albedo	0.50	Dimensionless
T_a	near-surface air temperature		K
T	ground or/and snow temperature		K
T_{s0}	ground or snow surface temperature		K
Z	total depth of the analysis domain		m
D_h	exchange coefficients for heat		Dimensionless
S	evaporation stress factor		Dimensionless
α_{pt}	Priestly-Taylor coefficient		Dimensionless
Δ	slope of the saturation vapor pressure temperature curve		$\mathrm{Pa\,K^{-1}}$
γ	psychrometric constant		$\mathrm{Pa\,K^{-1}}$
e_s	snow or soil surface vapor pressure		Pa
ε_s	surface emissivity	ground surface: 0.92 snow surface: 0.98	Dimensionless
P_a	atmospheric pressure		Pa
u_z	wind speed		$\mathrm{m\,s^{-1}}$
z_0	roughness length	ground surface: 0.015 snow surface: 0.001	m
ρ_{sn}	density of the snow	100–300	$\mathrm{kg\,m^{-3}}$

The turbulent exchange of sensible heat $\mathrm{Q_h}$ is given by Price and Dunne (1976):

$$Q_h = \rho_a c_p D_h (T_a - T_{s0}) \tag{4}$$

where $\rho_\mathrm{a} = 1.225\ \mathrm{kg\,m^{-3}}$ is the air density, $\mathrm{c_p} = 1004\ \mathrm{J\,kg^{-1}\,K^{-1}}$ is the specific heat of air, and $\mathrm{T_a}$ (K) is near-surface air temperature. The exchange coefficients for heat $\mathrm{D_h}$ $(-)$ can be estimated as:

$$D_h = \frac{\kappa^2 u_z}{\left(\ln\left(z/z_0\right)\right)^2} \tag{5}$$

where $\kappa = 0.4$ is the Von Karman's constant, $\mathrm{u_z}$ (m) is the wind speed at the instrument height z (m), and $\mathrm{z_0}$ (m) is the roughness length as $0.015\ \mathrm{m}$ for ground surface and $0.001\ \mathrm{m}$ for snow surface following Ling and Zhang (2004).

The latent heat flux was calculated via the Priestley-Taylor method (Priestley and Taylor, 1972).

$$Q_e = S \cdot \alpha_{pt} \frac{\Delta (Q_n - Q_c)}{\Delta + \gamma} \tag{6}$$

where S (–) is the evaporation stress factor, α_pt $(-)$ is the Priestly–Taylor coefficient, $\mathrm{Q_n}$ $(\mathrm{W\,m^{-2}})$ is the net radiation, Δ $(\mathrm{Pa\,K^{-1}})$ is the slope of the saturation vapor pressure-temperature curve, and γ $(\mathrm{Pa\,K^{-1}})$ is psychrometric constant. Δ is determined following Dingman (2015):

$$\Delta = \frac{4098 e_s}{(T_a - T_{frz} + 237.3)^2} \tag{7}$$

where $\mathrm{T_{frz}} = 273.15\ \mathrm{K}$ is the freezing point temperature, and $\mathrm{e_s}$ (Pa) is saturation vapor pressure derived following Dingman (2015):

$$e_s = 611 \exp\left(\frac{17.3\,(T_a - T_{frz})}{T_a - T_{frz} + 237.3}\right) \tag{8}$$

the γ is calculated using the formula proposed by Brunt (2011):

$$\gamma = \frac{c_p P}{\varepsilon L_v} \tag{9}$$

where P (Pa) is atmospheric pressure, $\mathrm{L_v} = 2.471 \times 10^6\ \mathrm{J\,kg^{-1}}$ is the latent heat of vaporization, and ε is a constant of 0.622 (Dingman, 2015). For each grid, the latent heat flux is treated separately for the bare ground surface, vegetation, and snow. The detailed parameterizations are in Appendix A. In current FPM, Monin-Obukhov similarity theory (for $\mathrm{Q_h}$) and Priestley-Taylor method (for $\mathrm{Q_e}$) were combined to improve simulation efficiency as some previous studies (Agam et al., 2010; Song et al., 2016). We acknowledge that using two different theories may introduce additional uncertainties.

Heat conduction through the snow layer or ground surface ($\mathrm{Q_c}$) was given as Liston and Hall (1995):

$$Q_c = (T_{s0} - T_g)\left(\frac{z_{sn}}{k_{sn}} + \frac{z_g}{k_g}\right)^{-1} \tag{10}$$

where $\mathrm{T_g}$ (K) is the ground temperature at the $\mathrm{z_g}$ depth, and $\mathrm{z_{sn}}$ is the thicknesses of snow (if present). The $\mathrm{k_{sn}}$ and $\mathrm{k_g}$ $(\mathrm{W\,m^{-1}\,K^{-1}})$ are the thermal conductivity of the snow and ground at the depth of $\mathrm{z_g}$, respectively.

The surface energy balance and heat conduction constitute a coupled non-linear equation system, and was solved iteratively for the surface temperature $\mathrm{T_{s0}}$, using the Newton-Raphson method.

2.2 Snow scheme

The significant influences of snow cover on soil thermal regime have been well documented (Zhang, 2005). Over the TP, snow cover is minor, with a mean annual snow depth of about 0.002 m (and about 0.01 m in winter) according to the ground observations from the China Meteorological Administration network (Orsolini et al., 2019; Cao et al., 2019b). Consequently, the snow effects are relatively minor in this region. The required degree of model complexity depending on the intended applications. For this reason, a simple snow scheme was incorporated into the initial version of FPM to represent the influences of seasonal snow on soil thermal regime. We acknowledge that the application of the FPM is not recommended in regions with prevalent snow due to its limited capability in simulating snow processes. The snow layer was discretized into multiple layers with a vertical resolution of 0.0025 m snow water equivalent for heat transfer simulations. The snow compaction algorithm from Verseghy (1991) was introduced here.

$$\rho_{sn}^{t+\Delta t} = (\rho_{sn}^{t} - \rho_{sn}^{max}) \cdot \exp(-0.24\Delta t) + \rho_{sn}^{max} \tag{11}$$

where $\rho_{\mathrm{sn}}^{\max} = 300\ \mathrm{kg\,m^{-3}}$ is the maximum snow density, and Δt is the simulation time step in day. The fresh snow density was set as $100\ \mathrm{kg\,m^{-3}}$.

The snow albedo is treated separately for non-melting and melting conditions following Douville et al. (1995). For non-melting conditions, a linear decrease is assumed for α_{sn}, while an exponential decrease is assumed for melting snow due to the presence of liquid water.

$$\alpha_{sn}^{t+\Delta t} = \begin{cases} \alpha_{sn}^{t} - 0.008\Delta t, & non-melting \\ \alpha_{sn}^{min} + (\alpha_{sn}^{t} - \alpha_{sn}^{min}) e^{-0.24\Delta t}, & melting \\ \alpha_{sn}^{max}, & \Delta snd \geq 0.01\ \mathrm{m} \end{cases} \tag{12}$$

where $\alpha_{\mathrm{sn}}^{\max} = 0.85$ denotes the maximum snow albedo or the fresh snow albedo, while $\alpha_{\mathrm{sn}}^{\min} = 0.50$ is the minimum snow albedo for old snow, and $\Delta\mathrm{snd}\ (\mathrm{m})$ refers to snow depth difference for simulation step. If there is a significant snowfall, i.e., $\Delta\mathrm{snd} \geq 0.01\ \mathrm{m}$, snow albedo was reset to the maximum by assuming the surface is completely overlaid by the fresh snow.

The snow cover fraction was given as

$$SCF = min\left(\frac{snd}{snd_{cr}},\ 1\right) \tag{13}$$

where snd (m) is the snow depth, and $\mathrm{snd_{cr}} = 0.1\ \mathrm{m}$ is the minimum snow depth that ensures complete coverage of the grid cell.

The snow volumetric heat capacity ($\mathrm{CV_{sn}}$, $\mathrm{J\,m^{-3}\,K^{-1}}$) and thermal conductivity are treated as functions of snow density (ρ_{sn}, $\mathrm{kg\,m^{-3}}$) following Douville et al. (1995):

$$CV_{sn} = CV_i \frac{\rho_{sn}}{\rho_i} \tag{14}$$

$$k_{sn} = k_i \left(\frac{\rho_{sn}}{\rho_w}\right)^{1.88} \tag{15}$$

where $\mathrm{CV_i} = 1.93 \times 10^6\ \mathrm{J\,m^{-3}\,K^{-1}}$ is volumetric heat capacity for ice, $\mathrm{k_i} = 2.22\ \mathrm{W\,m^{-1}\,K^{-1}}$ is the thermal conductivity of ice, $\rho_\mathrm{i} = 920\ \mathrm{kg\,m^{-3}}$ is ice density, and $\rho_\mathrm{w} = 1000\ \mathrm{kg\,m^{-3}}$ is water density. Snow ablation was heavily simplified by directly using the snow water equavalent from reanalysis. For the snow-melt season, if the snow temperature was found positive after conducting heat conduction, it was set to 273.15 K.

2.3 Ground heat conduction and phase change

The ground temperature T (K) changes over time (t) and depth (z, m), and is numerically solved by the heat conduction for energy transfer and phase change determined by Fourier's law:

$$C\frac{\partial T}{\partial t} = \frac{\partial}{\partial z}\left(k\frac{\partial T}{\partial z}\right) \tag{16}$$

The latent heat during phase change is taken into account through an apparent volumetric heat capacity:

$$C = CV_s + L\frac{\partial \theta_u}{\partial T} \tag{17}$$

where C and $\mathrm{CV_s}$ are the apparent volumetric heat capacity and volumetric heat capacity of soil ($\mathrm{J\,m^{-3}\,K^{-1}}$), respectively, L ($\mathrm{J\,m^{-3}}$) is the volumetric latent heat of fusion for ice, and θ_u ($\mathrm{m^3\,m^{-3}}$) is the volumetric unfrozen water content or supercooled water. The unfrozen water was parameterized following Niu and Yang (2006):

$$\theta_u = \theta_{sat}\left\{\frac{10^3 L_f\,(T - T_{frz})}{gT\psi_{sat}}\right\}^{-\frac{1}{b}} \tag{18}$$

where θ_sat ($\mathrm{m^3\,m^{-3}}$) is the saturated soil moisture, $\mathrm{L_f} = 0.334 \times 10^6\ \mathrm{J\,kg^{-1}}$ is mass specific latent heat of water, $\mathrm{g} = 9.80665\ \mathrm{m\,s^{-2}}$ is the acceleration due to gravity, ψ_sat (mm) is the saturated soil matric potential depending on the soil material properties, and b is the Clapp-Hornberger parameter (Appendix B). FPM implements the nonlinear heat-transfer equations in Cartesian coordinates.

Thermal properties of the soil are assumed to be a weighted combination of different components of the soil column. The $\mathrm{CV_s}$ is calculated from the volumetric fractions of the constituents as follows Westermann et al. (2016):

$$CV_s = \sum_n f_n CV_n \tag{19}$$

where subscripts $\mathrm{n} = \mathrm{m}$, o, w, i, a, and g refer to soil constituents of mineral, organic, water, ice, air, and gravel. In this context, $\mathrm{f_n}$ ($\mathrm{m^3\,m^{-3}}$) and $\mathrm{C_n}$ ($\mathrm{J\,m^{-3}\,K^{-1}}$) represent the volumetric contents and the volumetric heat capacities for each component (Table E1). Similarly, the thermal conductivity of the soil $\mathrm{k_s}$ ($\mathrm{W\,m^{-1}K^{-1}}$) is calculated based on their composition following Cosenza et al. (2003):

$$k_s = \left(\sum_n f_n \sqrt{k_n}\right)^2 \tag{20}$$

where $\mathrm{k_n}$ is the thermal conductivity ($\mathrm{W\,m^{-1}K^{-1}}$) for each soil component (Appendix E).

3 Model setting up and ensemble simulation

3.1 Soil profile

We adopted the general principle for soil discretization–the grid size increases with depth–to maintain numerical stability and reduce computational cost. The soil column is discretized to 172 layers with a total depth of 150 m. The soil vertical grid size increased from 0.01 m for subsurface to 5.0 m for deep soil (Table D1). We use the soil texture of the Global Soil Dataset for Earth System Models (GSDE) from Dai et al. (2019) as it additionally provides the soil gravel content, which is prevalent over the TP. GSDE has 8 soil layers with a total depth of 3.8 m. The information of the last layer was extended to deeper soil, but was further refined based on the bedrock dataset from Shangguan et al. (2017). Note that, we assume soil organic matter is absent for soil below 3 m as is normally done in Earth system models (c.f., Chadburn et al., 2015).

3.2 Soil water content

Soil moisture can significant affect the dynamics of the soil thermal regime through evapotranspiration and by altering soil thermal properties (Göckede et al., 2017; Zwieback et al., 2019). However, in the permafrost regions of the TP, soil moisture exhibits marked heterogeneity and is difficult to accurately represent in models. This challenge stems from uncertainties in soil datasets and climate forcing, as well as the inherent complexities of the rugged terrain. For the current version, the static soil moisture is used. To specify the vertical water distribution within the soil column, we used sub-grid parameterizations from SURFEX and CryoGridLite (Decharme et al., 2006; Masson et al., 2013; Langer et al., 2024). Here, we distinguished four hydrological layers in the subsurface, from the uppermost surface to deep layer, including the: 1) root zone; 2) vadose layer, extending from the root layer downward to the lower boundary or saturated table/bedrock (if present); 3) saturated layer, which lies between the depth of groundwater table and bedrock; and 4) bedrock layer, extends down to the lower boundary. Note that the presence and depth of the saturated layer is estimated based on the groundwater table information from Fan et al. (2013). The root depth is set between 0.05 m for bare soil and 0.5 m for high vegetation, and the typical depth for different vegetation cover is from GEOtop (Endrizzi et al., 2014).

In the root layer, the water content θ_{R} ($\mathrm{m}^3\,\mathrm{m}^{-3}$) is estimated as the ensemble mean of five remote sensing-based products (Table 2, details see Sec. 3.3). The water content for the vadose layer θ_{v} ($\mathrm{m}^3\,\mathrm{m}^{-3}$) is determined based on field capacity θ_{fc} ($\mathrm{m}^3\,\mathrm{m}^{-3}$) and soil porosity ϕ ($\mathrm{m}^3\,\mathrm{m}^{-3}$), and an ensemble range is used (see Sec.3.3). Please see Appendix B for the parameterizations of soil properties. In the saturated layer, the water content (θ_{sat}) is equal to ϕ. The water content of 0.05 $\mathrm{m}^3\,\mathrm{m}^{-3}$ was used for the bedrock (Gubler et al., 2013).

3.3 Ensemble simulations for soil hydrology

Although the use of static soil moisture models is common practice for investigating long-term permafrost changes among permafrost researchers (e.g., Jafarov et al., 2012; Qin et al., 2017; Langer et al., 2024), and four vertical water distribution schemes were implemented in FPM to reduce the uncertainties associated with static soil moisture, this estimate is subject to

Table 2. Climate forcing and input datasets used in Flexible Permafrost Model (FPM).

Input parameter	Dataset	Period	Resolution	Source/reference
Climate forcing	ERA5-Land	1950–2023	0.10°	Muñoz-Sabater et al. (2021)
		Surface cover		
Vegetation optical depth	VOD Climate archive	2002–2018	0.25°	Moesinger et al. (2020)
Leaf area index	Reprocessed MODIS version 6.1 LAI	2000–2021	0.05°	Myneni et al. (2021)
Vegetation type	1:1 million vegetation map of China	static	1/120°	Hou (2019)
Surface albedo	Global surface blue-sky albedo	2001–2020	0.05°	Jia et al. (2022)
		Soil profile and moisture		
Surface soil moisture	ASCAT	2007–2022	0.11°	SAF (2020)
	AMSR2–LPRM	2012–2023	0.25°	Parinussa et al. (2015)
	ESA CCI SM	2000–2022[1]	0.25°	Dorigo et al. (2017)
	SMOC–IC	2010–2021	0.25°	Fernandez-Moran et al. (2017)
	SMAP–L3	2015–2023	0.37°×0.44°	O'Neill et al. (2021)
Soil texture	Global Soil Dataset for Earth System Models	static	1/120°	Dai et al. (2019)
Bedrock depth	Global depth to bedrock	static	1/120°	Shangguan et al. (2017)
Watertable depth	Groundwater table depth	static	1/120°	Fan et al. (2013)
Geothermal heat flux	Global Map of Solid Earth Surface Heat Flow	static	2°	Davies (2013)

[1] To be consistent with the other soil moisture products, only the period of 2000–2022 are used here, although ESA CCI provides a longer period.

large uncertainty. To allow the propagation of this uncertainty into model results, we introduced both wetter and drier variants of the default parameters (see Sec. 3.3). The ensemble simulations–allowing degrees of parameter uncertainties–are widely used for Earth system studies as they generally outperform individual simulations (Cao et al., 2019a; Langer et al., 2024). In this study, the ensemble simulation is produced using reasonable ranges of parameters (Table 3). Both the ensemble range of soil moisture in root layer and vadose zone are assumed here to allow possible uncertainties. The θ_{R} is derived as an ensemble mean of five state-of-the-art products (Table 2), and the ensemble was produced by $\pm$ standard deviation of all these products. The baseline of θ_{v} was determined as the mean of θ_{fc} and θ_{sat} in previous studies (e.g., Langer et al., 2024). This means the soil moisture in the vadose layer is in the middle of θ_{fc} and θ_{sat}, coincidentally. We followed this algorithm, but allowed the propagation of uncertainty into model results. This is qualitatively described by a dry and wet variants of the θ_{v} parameter used (Table 3). We emphasize that the ensemble was chosen after considerable tests and comparisons but ultimately remains a subjective choice at this time. The range of the above selected parameters are used for the 45-member ensemble simulation to represent a wide range of permafrost conditions.

Table 3. Soil moisture ($\mathrm{m}^3\ \mathrm{m}^{-3}$) parameters selected for ensemble simulations. The dry and wet variants indicate the parameter ensemble range, and default indicates the standard choice used in model simulation.

Soil layer	Root layer	Vadose layer
Symbol	θ_R	θ_v
Default	ensemble mean[1]	$\frac{\theta_{\mathrm{sat}}+\theta_{\mathrm{fc}}}{2}$
Dry	$-$std.[2]	$-0.1(\theta_{sat}-\theta_{fc})$
Wet	$+$std.	$+0.1(\theta_{\mathrm{sat}}-\theta_{\mathrm{fc}})$
Step	$\frac{\mathrm{std.}}{4}$	$0.05(\theta_{\mathrm{sat}}-\theta_{\mathrm{fc}})$

The footnote of [1] and [2] mean the ensemble mean and standard deviation (std.) of five remote-sensing-based soil moisture in Table 2.

3.4 Model settings

The simulation was conducted at a time step of 1 day. A lower boundary condition of geothermal heat flux from Davies (2013) is used (Table 2). To ensure the convergence of soil temperature profile, the model was initialized through a 1000-year spin-up process. This was achieved by cyclically applying the climate forcing data from the first decade (July 1950 to June 1960) one hundred times. Simulation performance was measured by the mean bias (BIAS) as well as root mean square error (RMSE), and more details can be found in Appendix C.

3.5 Diagnosis and analyses of permafrost characteristics

The permafrost is diagnosed following its definition, i.e., the daily soil temperature of a simulation pixel remains at or below 0 $^\circ\mathrm{C}$ for two or more years at given depth. Instead of directly using presence/absence of permafrost for individual ensemble member, the permafrost zonation index (PZI), as a fraction (0–1) corresponds to the 45 simulation members identified the probability of permafrost presence for each grid, is introduced to represent permafrost extent here. In such, the PZI can be used to quantitatively explore permafrost changes for each grid. More details of permafrost probability estimate could be found from Obu et al. (2019); Burke et al. (2020). In this study, we especially focus on the thermal state of permafrost at a depth of 3 m as the near-surface permafrost treated in most land surface models (Burke et al., 2020), and 15 m as the permafrost mean annual ground temperature (MAGT). The permafrost extent for above 100 m is additionally used as reference. The glaciers and lakes from ERA5-Land are masked before permafrost extent analyses. The ALT is estimated from linear interpolation of daily soil temperature. In this study, the period of 2010–2023 is used as the current condition for permafrost.

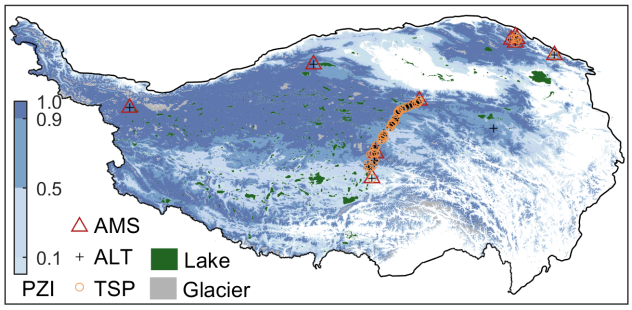

Figure 1. *In situ* observations used for model evaluation, including comprehensive observation sites with both the active layer soil temperature and atmospheric observations from the automatic meteorological system (AMS), active layer thickness (ALT) from soil temperature profile, and the permafrost thermal state (TSP) from boreholes. The permafrost zonation index (PZI) is from Cao et al. (2019b).

Table 4. Metadata for the synthesis sites with both permafrost and atmospheric forcing measurements, including latitude (Lat, ° N), longitude (Lon, ° E), elevation (Ele, m), vegetation type, mean soil moisture (SM, $\mathrm{m^3\,m^{-3}}$) in growth season, mean annual ground temperature (MAGT, °C), active layer thickness (ALT, m), and measurement period.

Site	Lat	Lon	Ele	Vegetation	MAAT	SM	MAGT	ALT	Period	References
AYK	37.54	88.80	4300	Alpine desert	−5.2	0.05	−3.40	/	2014–2018	
LDH	31.82	91.74	4808	Alpine swamp meadow	−2.3	0.41	/	1.2	2002–2018	
TGL	33.07	91.94	5100	Alpine meadow	−4.7	0.14	−1.15	3.3	2006–2013	Zhao et al. (2021)
TSH	35.36	79.55	4740	Alpine desert	−6.0	0.09	−2.63	1.0	2015–2019	
XDT	35.72	94.13	4538	Alpine meadow	−3.6	0.32	−0.54	1.4	2011–2018	
EboA	38.00	100.92	3691	Alpine swamp meadow	−2.6	0.66	−0.68	0.8	2011–2021	
PT1	38.78	98.75	4128	Alpine swamp meadow	−7.4	0.40	−1.76	1.6	2011–2021	
PT5	38.81	99.03	3691	Alpine meadow	−2.3	0.33	0.03	3.6	2011–2021	Cao et al. (2018)
PT6	38.95	98.96	4153	Alpine meadow	−5.1	0.36	−1.62	2.5	2014–2021	
PT9	38.63	98.95	3970	Alpine swamp meadow	−4.2	0.50	−1.38	1.9	2014–2021	

4 Data

4.1 Climate forcing

FPM is driven by climate forcing from reanalysis, including: near-surface air temperature, wind speed, incoming shortwave radiation, incoming longwave radiation, atmospheric pressure, and snow water equivalent. In FPM, the historical climate is taken from the ERA5-Land datasets, produced by the European Centre for Medium-Range Weather Forecasts (ECMWF, Table 2). ERA5-Land is an enhanced land component of ERA5 with a spatial resolution of 0.1° and a coverage from 1950 to the present (Muñoz-Sabater et al., 2021). The reanalyses were evaluated against the in situ observations (Appendix D). Note

that the snowfall from ERA5-Land was reported to be over biased due to the significant drawback of precipitation represented in models (Orsolini et al., 2019). For this reason, the simulated snow influences on soil thermal regime were very likely artificial amplified.

4.2 Surface cover

FPM considers the influences of vegetation on permafrost via the latent heat and soil moisture etc. (Appendix A). In FPM, static vegetation is assumed and the vegetation optical depth (VOD), leaf area index (LAI), and vegetation type are required (Table 2). For snow-free periods, the ground albedo is from Jia et al. (2022).

The remote-sensing datasets vary in their temporal coverage, so we used the climatology to represent the long-term conditions. For the VOD and snow-free ground albedo, the daily measurements over the entire recording period were aggregated into a day-of-year climatology using the median, so as to reduce sensitivity to extreme values. The monthly LAI from Myneni et al. (2021) was aggregated to monthly medians. Daily θ_{R} values were first aggregated into monthly averages for each dataset. These monthly values from the thawing season (June to August) were then used to compute the annual mean. For each soil moisture dataset, the average over the entire recording period was derived, and an ensemble mean across the five datasets was calculated and employed as model inputs. Note that only the measurements from the thawing season (June to August) were used to derive VOD and θ_{R}).

4.3 Datasets used for model evaluation

4.3.1 Synthesis datasets

In this study, 10 synthesis sites with both meteorological and soil temperature measurements were used to conduct the detailed evaluations (Table 4, Fig. 1). The soil information, i.e., soil texture and moisture are also available at the sites. Note that the missing atmospheric observations are filled with downscaled reanalyses following the algorithm presented by Fiddes and Gruber (2014); Cao et al. (2017a).

4.3.2 Active layer thickness and borehole temperature

Active layer thickness and borehole temperature measurements from the Global Terrestrial Network for Permafrost (GTN-P, Biskaborn et al., 2019) and literature (see Supplement for details) are used here to evaluate model performance. This yielded 247 ALT measurements from 128 sites (Fig. 1). The measured mean ALT was about 2.3 ± 0.8 m with a range of 0.7–4.9 m. ALTs are derived from different land covers, including Alpine desert, alpine steppe, alpine meadow, and alpine swamp meadow, indicating that the evaluation presented here is representative.

The MAGT measurements between the depths of 7.5 and 40 m are treated as the thermal state of permafrost, and this leads to 71 boreholes with 364 MAGT measurements that were used for model evaluation. The measured mean MAGT was about -0.95 ± 1.1 $^{\circ}\mathrm{C}$ with a range from -4.2 to 2.2 $^{\circ}\mathrm{C}$. Among the measurements, 18 borehole sites with a long times-series (≥ 1 decade) were further used to evaluate the modeled TSP changes.

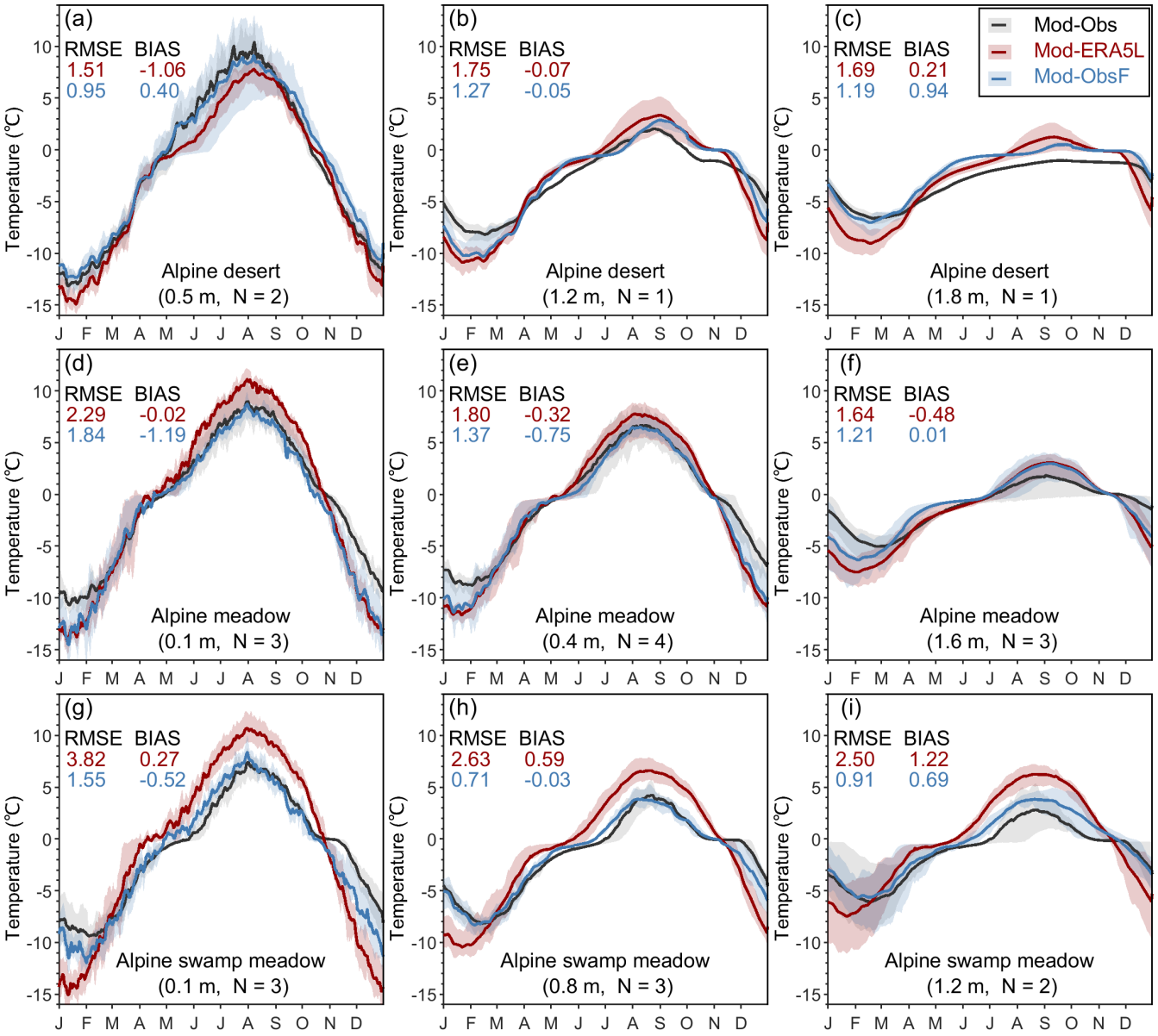

Figure 2. Comparison of simulated and observed day-of-year soil temperature in the active layer across the synthesis sites. The daily soil temperature present is averaged for each vegetation type and soil depth based on all available sites and years. The soil depth and numbers of sites (N) are given in parentheses. The sites used for each vegetation type and depth differ based on data availability. Observations are in black, red lines show the simulation forced by reanalyses, and the blue lines represent that forced by observed atmospheric forcing and *in situ* soil information (if available). The shaded areas depict the ensemble range from the 25th to 75th. The ensemble of observation forced simulation are produced using results from different sites and additional ranges of soil moisture (see Table 3).

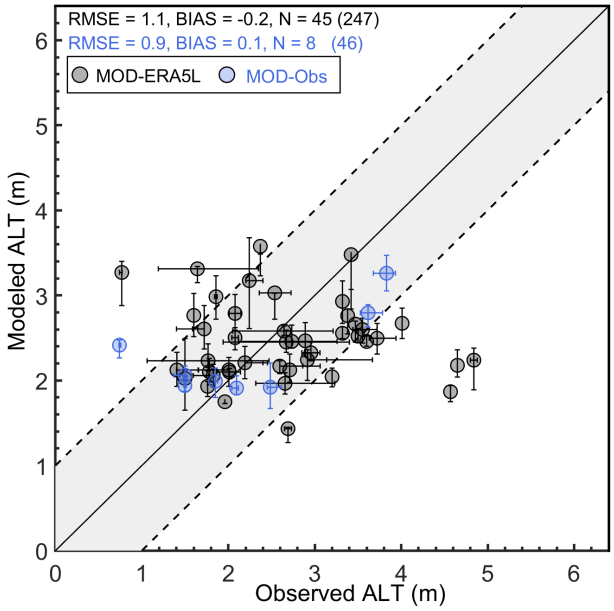

Figure 3. Evaluation of modeled active layer thickness (ALT). The ensemble mean from FPM simulations (MOD-ERA5L) are given in black dot, with the whiskers representing the range between the 25th and 75th percentiles. The observed mean was aggregated from multiple measurements at a single site or from multiple sites within the same grid. N indicates the number of grids used for evaluation after aggregating sites within the same grid, and the number of measurements was given in parentheses. The additional simulation driven by observed meteorological forcing (MOD-Obs) are given in blue. Dashed lines indicate $\pm$ 1 m.

4.3.3 Referenced permafrost distribution

We use five permafrost maps as reference datasets to evaluate the modeled permafrost area. These are (1) the new map of permafrost distribution on the TP via the semi-physical 'temperature at the top of permafrost' (TTOP) model (Zou et al., 2017); (2) the permafrost zonation index map compiled based on the statistical relationship between topoclimatic predictors (e.g., air temperature, snow, and vegetation) and permafrost zonation (Cao et al., 2019b); (3) the global permafrost zonation index with the normal and cold variant (Gruber, 2012); (4) the Northern Hemisphere permafrost map derived via the TTOP model (Obu et al., 2019), and (5) the outputs from LSM of Noah-MP (Wu et al., 2018). The permafrost extent from these maps is estimated for different time periods using different modeling paradigms and are not perfect or a 'source of truth'. We treat them as an ensemble and use their range and mean as the 'best available' reference.

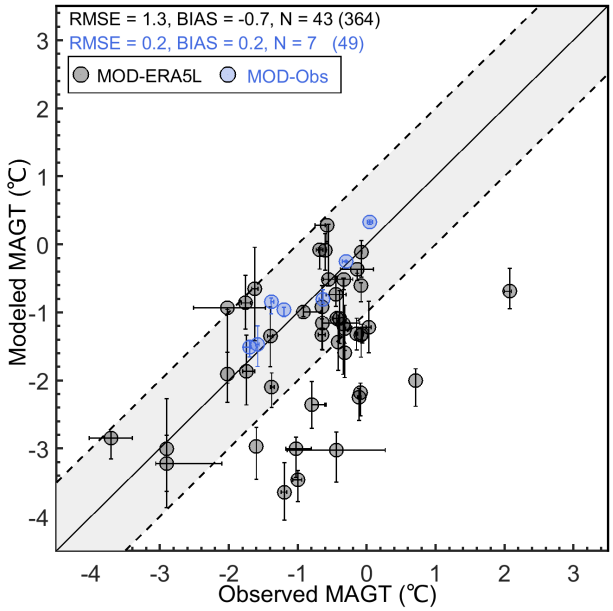

Figure 4. Same as Figure 3, but for the mean annual ground temperature (MAGT). Dashed lines indicate $\pm$ 1 $^{\circ}$C.

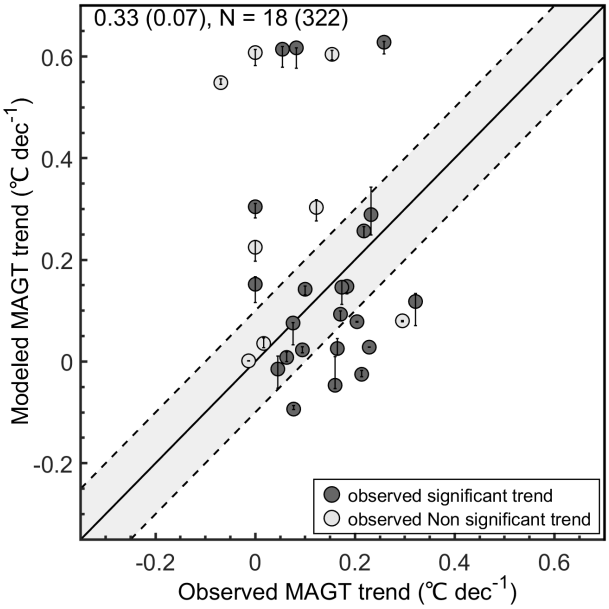

Figure 5. Same as Figure 3, but for the mean annual ground temperature (MAGT) changes. Only the sites with long-term observations ($\geq$ 1 decade) are used here. The filled dots are sites with observed significant trends. Dashed lines indicate $\pm$ 0.1 $^{\circ}$C dec^{-1}.

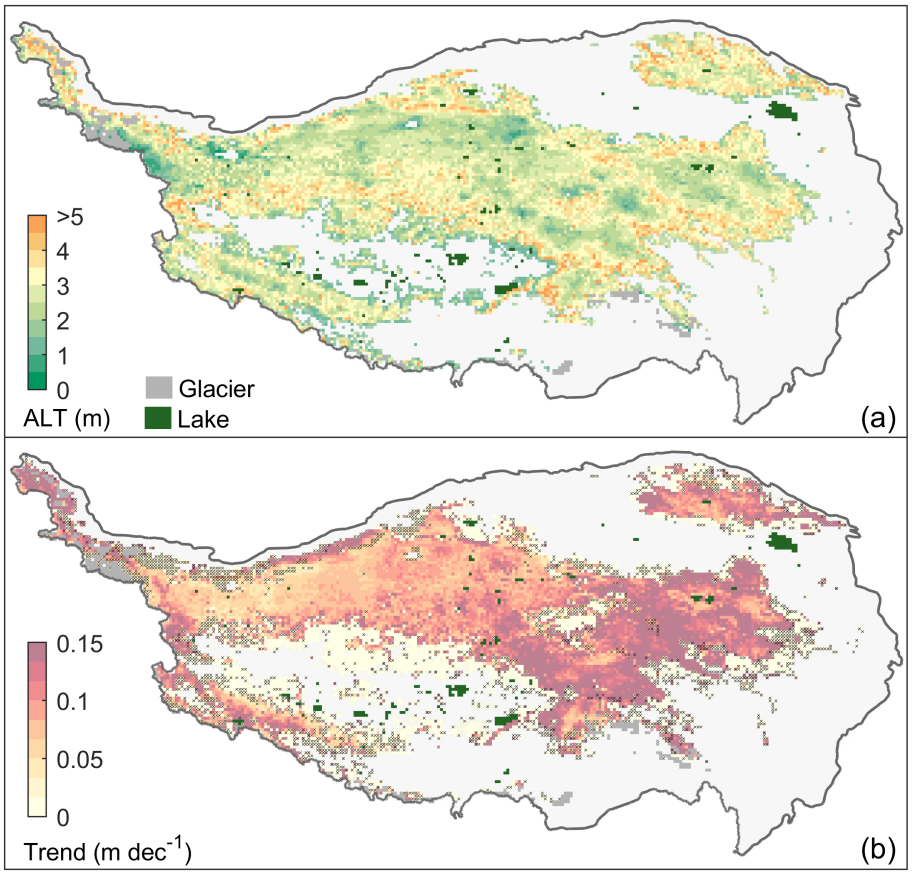

Figure 6. (a) The modeled current (2010–2023) mean active layer thickness (ALT), and (b) its change rate from 1980 to 2023. The areas without significant trends are marked by ×. Glaciers and lakes are from ERA5-Land.

5 Results

5.1 Model evaluations

Our evaluation results showed the overall RMSE of daily soil temperature in the active layer was 2.2 °C with a BIAS of 0.2 °C (Figure 2). FPM showed relatively worse performance in areas with alpine swamp meadow (RMSE = 3.0 °C), with warm bias in summer and cold bias in winter. This is attributed to poorly prescribed soil information, i.e., peat layer and soil moisture. At the sites with alpine desert, the overestimated soil moisture (by about 25%) at 0.5 m depth leads to a colder simulated soil temperature in summer (Figure 2a). To demonstrate the hypothesis, we conducted the additional simulations using observed atmospheric forcing and soil profile from borehole measurements. The simulated soil temperature was significantly improved by 2.0 °C, indicating FPM could be improved with more reliable climate forcing and soil profile (Fig. 2).

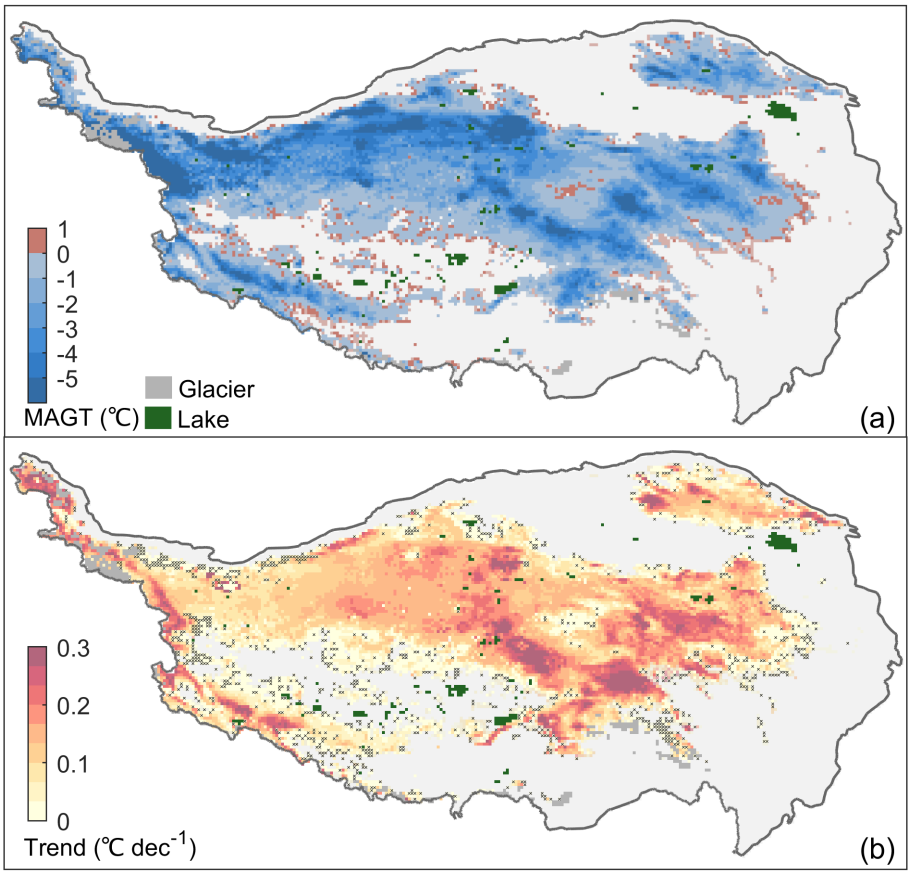

Figure 7. (a) The modeled current (2010–2023) mean annual ground temperatures at the depth of 15 m, and (b) its change rate from 1980 to 2023. The areas without significant trends are marked by ×.

FPM generally has good agreement with observed ALTs with the overall RMSE of 1.1 m, and slightly underestimated ALT (BIAS = −0.2 m) due to the cold-biased summer air temperature (Fig. 3 and D1). Following the relatively worse soil temperature, ALT was over-biased in areas with alpine swamp meadow. The additional simulation with observed forcing and soil information, again, showed more promising results (RMSE = 0.9 m). The ALT bias was within ± 1 m at most (67 %) evaluated cells (Fig. 3).

FPM is found to underestimate the MAGT with an overall mean BIAS of −0.7 °C, which is aligned with the cold-biased air temperature (Fig. D1a and d). The overall MAGT RMSE was 1.3 °C (Fig. 4), and about 61 (82)% sites have a bias within ± 1 (2) °C. Although the MAGT change trend is well addressed by FPM with an RMSE of 0.33 °C dec^{-1}, it is found even greater than the observed mean MAGT trend of 0.12 ± 0.09 °C dec^{-1} (Fig. 5). This indicates that the simulated MAGT trend may not be reliable. In fact, the permafrost warming at the measured sites was relatively gentle (with a range from −0.07 to 0.3 °C dec^{-1}) compared to that in high latitudes (Hock et al., 2019). This is because the permafrost temperature over the TP is

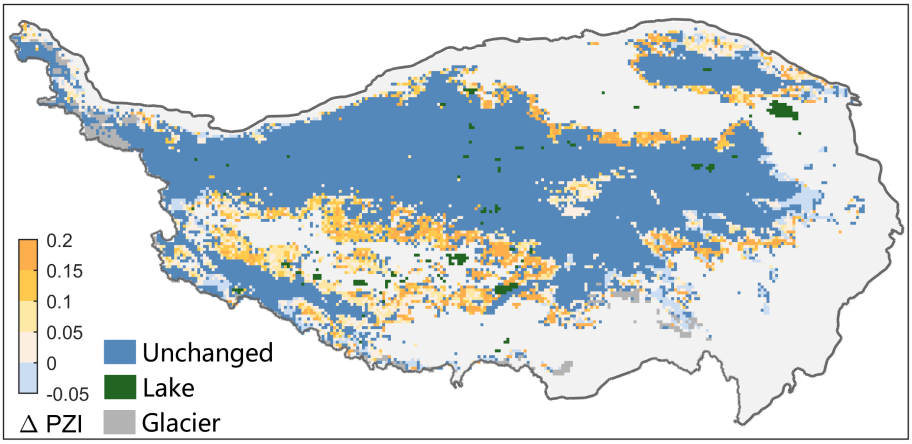

Figure 8. Changes of permafrost extent between 1991–2020 and 1951–1980. The permafrost zonation index (PZI) are 45-member ensemble probability of permafrost where permafrost is defined by the daily temperature at 15 m depth.

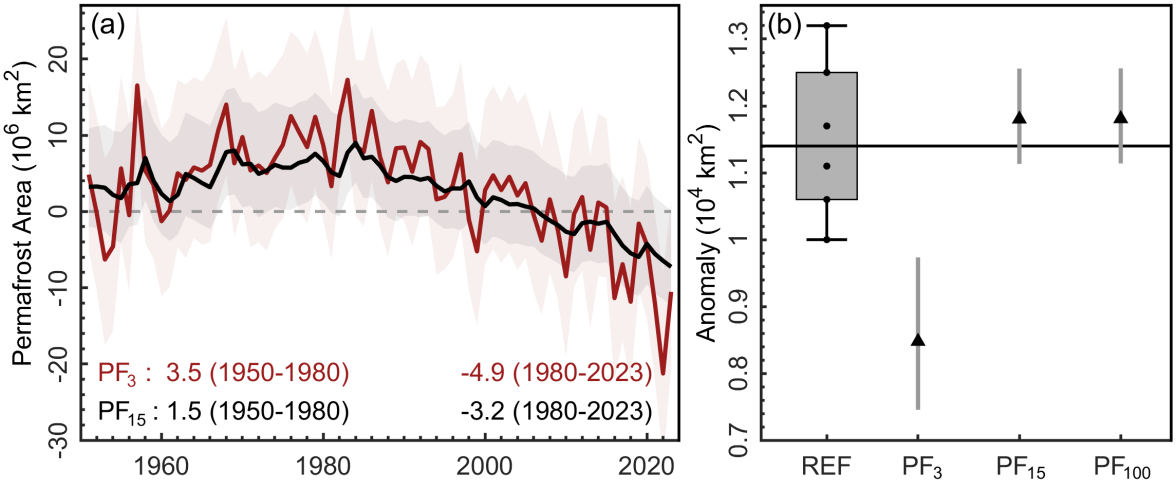

Figure 9. (a) Comparison of estimated current (2010–2023) permafrost area from FPM simulations with referenced estimations, and (b) anomaly of permafrost area since 1950. The subscript means the depth above which permafrost is diagnosed. The permafrost area trend (10^4 km^2 dec^{-1}) is estimated for the periods before and after 1980, separately.

very "warm", and the heat from atmosphere was consumed by phase change rather than temperature increase (also see Fig. 7).
300 The significant latent heat introduce additional challenge for reproducing MAGT trend.

Excluding glaciers and lakes, the estimated current (2010–2023) permafrost area was about $1.18 \pm 0.02 \times 10^6$ km^2 based on the ensemble simulations from FPM. This is found reasonable compared to the referenced ensemble mean of $1.15 \pm 0.12 \times 10^6$ km^2 (Fig. 8). In addition, our model performance and simulated ALT, MAGT, and permafrost extent are comparable to the stand-alone model of CryoGridLite (Chen et al., 2025).

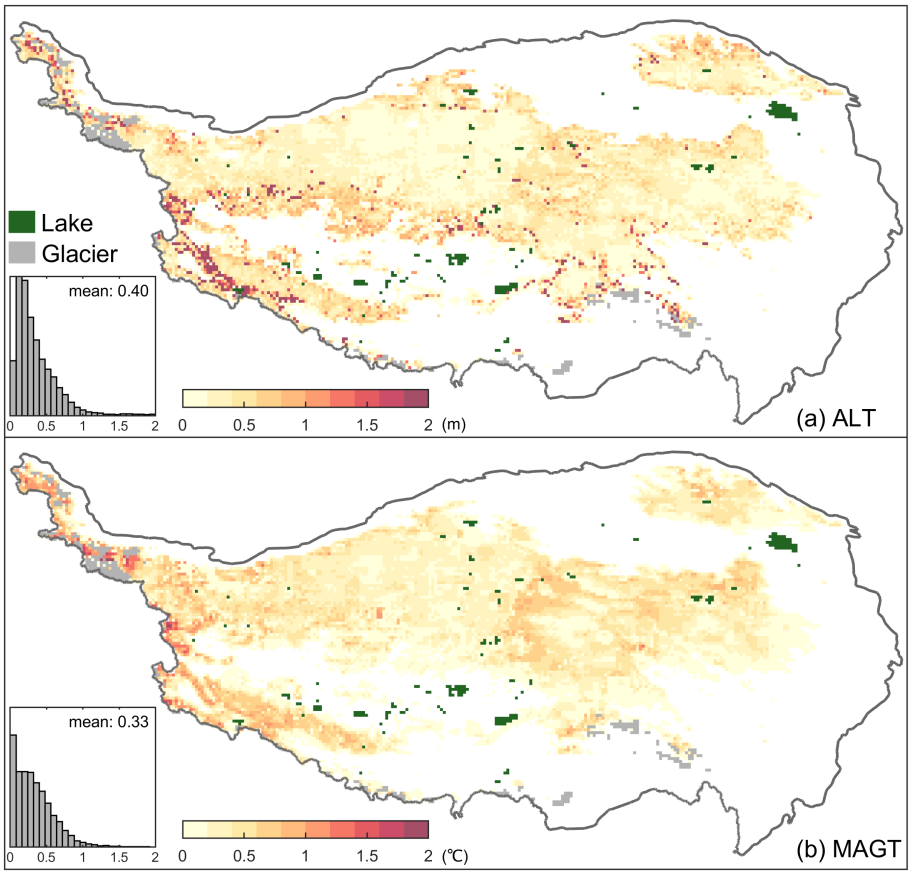

Figure 10. The standard deviation of (a) simulated active layer thickness (ALT) and (b) mean annual ground temperature (MAGT) based on the 45-member ensemble simulations which accounted the possible soil moisture spread in root and vadose zones.

5.2 Changes in active layer thickness

The ensemble simulations from FPM showed the current (2010–2023) overall mean ALT was about 2.79 ± 0.86 m over the TP. The results are found highly align with the geothermal model, i.e., 2.1–2.4 m, from Qin et al. (2017). Our results indicated that about 39.1 % of permafrost regions have an ALT greater than 3 m, highlighting that the widely used land surface models and reanalyses with shallow soil column may not be sufficient for permafrost studies over the TP. The long-term simulation showed that ALT had a inter-annual trends with a decreasing trend between 1950 and 1980 (-0.04 m dec^{-1}), followed by a dramatically continuous increasing trend (0.06 m dec^{-1}). Consequently, the ALT over TP increased by 0.22 m since 1980 (Fig. 6b).

5.3 Changes in permafrost temperature

The mean annual ground temperature at the depth of 15 m (MAGT_{15}) is used to represent the thermal state of permafrost. The modeled overall mean MAGT_{15} (2010–2023) was about -2.0 ± 2.1 $^{\circ}\mathrm{C}$ for the permafrost regions over the TP and shows a wide range from -18.0 to 2.5 $^{\circ}\mathrm{C}$ (Fig. 7a). Our simulations revealed that the overall MAGT_{15} increased by approximately 0.22 $^{\circ}\mathrm{C}$ since 1950, with a more dramatic warming of 0.28 $^{\circ}\mathrm{C}$ (or 0.06 $^{\circ}\mathrm{C\,dec^{-1}}$) since 1980. Similar to the ALT, MAGT shows a clear cooling trend (-0.01 $^{\circ}\mathrm{C\,dec^{-1}}$) between 1950 and 1980 corresponding to the changes in near surface air temperature.

5.4 Changes in permafrost extent

The permafrost area decreased by approximately 10.5 $\times$ $10^4\,\mathrm{km^2\,dec^{-1}}$ during 1950–2023, but increased by 2.6 $\%$ from 1950 to 1980 following cooling of the near-surface air temperature (Fig. 9b). Permafrost area decreased at a rate of 3.2 $\times$ $10^4\,\mathrm{km^2\,dec^{-1}}$, or a total area of 10.8 $\%$, since 1980. Our results showed that the model with shallow soil column would significantly underestimate permafrost area but overestimated permafrost degradation. Take the top 3 m as an example, which has been widely used in the land surface model. The estimated near-surface (top 3 m) permafrost area (8.46 $\times$ $10^4\,\mathrm{km^2}$) was about 26.5 $\%$ smaller compared to the ground "truth", or 28.3 $\%$ smaller than the simulations with sufficient soil column (e.g., 100 m, Fig. 9a). In addition, the permafrost degradation was overestimated by about 53 $\%$ (3.2 $\times$ $10^4\,\mathrm{km^2\,dec^{-1}}$ $vs.$ 4.9 $\times$ $10^4\,\mathrm{km^2\,dec^{-1}}$) with shallow soil column (Fig. 9). This highlights that the current land surface models with shallow soil column can lead to significant uncertainties in permafrost simulations.

5.5 Simulation spread

The ensemble simulation revealed that the variation in soil moisture translated into considerable influences on simulated permafrost characteristics (Fig. 10), with the overall mean standard deviation was about 0.4 m in ALT and about 0.33 $^{\circ}\mathrm{C}$ in MAGT. Notably, the input soil moisture datasets themselves exhibited substantial variability, with mean standard deviation of 0.11 $\mathrm{m^3\,m^{-3}}$ in root zone and 0.14 $\mathrm{m^3\,m^{-3}}$ in vadose zone (Fig. D2). The propagation of input uncertainties into significant permafrost simulation bias thus highlights the essential role of obtaining more reliable soil moisture datasets for advancing our capacity to simulate permafrost changes.

6 Discussions

6.1 Uncertainties from climate forcing and input datasets

We used the ERA5-Land reanalyses as model forcing. However, the ERA5-Land is found cold biased in near-surface air temperature (Appendix D, Fig. D1), leading to underestimated ALT as well as MAGT (Fig. 6 and 7). In fact, permafrost simulations are hampered by reduced reanalyses quality in cold regions primarily due to inherent challenges in representing nonlinear processes involving ice, or its phase change near 0 $^{\circ}\mathrm{C}$ (Cao and Gruber, 2025). The poorly described soil column, especially the soil organic matter, put additional uncertainty for permafrost simulations.

6.2 Model limitations

In this study, we introduced and demonstrated the suitability of FPM for large-scale permafrost simulation. For the initial version of FPM, there are four main limitations. First, the snow scheme is simplistic, although significant influences of snow cover on soil thermal regime have been well documented (Zhang, 2005). FPM currently does not consider the snow mass balance, and, therefore, additionally requires snow water equivalent as input. Further, the snow cover fraction used here was developed for high latitudes and does not consider the influences of complex terrain, which may redistribute the snow cover and lead to strong heterogeneity for the soil thermal regime. While the simple snow scheme seems adequate for the Tibetan Plateau with little snow, considerable efforts are required to improve snow processes if FPM would applied to snow-prevalent areas, i.e., the high latitudes.

Second, FPM does not consider the water balance, and the static surface conditions, including vegetation and albedo (varies with season but remains unchanged among years), were assumed via using the remote-sensing-based climatology. This means the influences of surface and sub-surface changes are not accounted for and limited the model ability in predicting long-term permafrost changes.

Third, the fine-scale influences (i.e., debris and peat layer) are either not or simply represented here due to the simulation scale ($\sim$10 km). This may overestimate permafrost degradation, especially for the areas near the permafrost lower limit, where the relict permafrost was found (Fig. 8, Cao et al., 2021).

Fourth, FPM does not consider the thermokarst processes or the so-called "abrupt thaw" raised by excess ice loss. The thermokarst was thought as local-scale tipping element that would remarkably accelerate permafrost degradation (Devoie et al., 2019).

6.3 Comparison with other permafrost models

Our results are found comparable to previous simulations derived from the geothermal numerical models (e.g., Qin et al., 2017; Chen et al., 2025) as well as land surface models (e.g., Guo and Wang, 2013; Wu et al., 2018; Zheng et al., 2020). FPM, as the stand-alone permafrost model, benefits from the consideration of land-atmosphere processes (i.e., the surface energy balance and vegetation effects) typically not included in geothermal numerical models, while maintaining the deep soil column and suitable numerical solver for soil phase change. In addition, the land-surface-scheme designed structure and streamlined processes (i.e., its efficient simulation of latent heat) make it suitable for large-scale ensemble simulations. Different from the other land surface scheme models with rich processes beyonds permafrost, such as SUTRA (McKenzie et al., 2007), Advanced Terrestrial Simulator (Jan et al., 2020), and CryoGrid 3 (Westermann et al., 2023), which are applied to fine scales, the initial FPM aim to provide a flexible yet simple platform for large-scale permafrost simulation studies.

6.4 Future developments

Previous studies reported that the permafrost processes of the Earth system model in CMIP6 is limited improved compared to the previous generation of CMIP5 (e.g., Burke et al., 2020), and current Earth system models generally have weak ability in

representing permafrost (Schädel et al., 2024). This highlights the urgent need to develop the stand-alone permafrost model. Since the required inputs are derived from global datasets, this opens the opportunity for global permafrost simulation with the FPM platform. The incorporation of a state-of-the-art snow scheme – particularly critical for high-latitude permafrost processes – will further enhance this capability. We hope with improved permafrost ground ice maps and a rigorously validated solution (addressing both physical processes and numerical solver aspects), we can implement excess ice loss processes within FPM to represent permafrost "abrupt thaw". Thermokarst features, such as thaw slumps, ponds, and lakes, are considered local-scale tipping elements in permafrost thawing. We hope FPM could be further improved via incorporating lateral heat transfer, as described by Sun et al. (2023), making FMP a cross-scale platform for understanding diverse permafrost landscapes.

7 Conclusions

In this study, we introduce a new land surface scheme specifically designed for permafrost applications, the Flexible Permafrost Model (FPM). This model serves as a flexible platform to explore novel parameterizations for a variety of permafrost processes. To demonstrate the utility of FPM for supporting permafrost studies, we apply the model to permafrost studies over the Tibetan Plateau. Our simulation results are compared to *in situ* observations and published permafrost extent. We summarize the main contributions and insights of this work as the following:

1. FPM shows suitability in reproducing permafrost characteristics, such as active layer thickness, and the thermal state. With more reliable inputs, especially soil profile, FPM-based simulations can be further improved;

2. Simulations indicated that the current (2010–2023) mean active later thickness was about $2.79 \pm 0.86\ \mathrm{m}$, permafrost temperature at a depth of $15\ \mathrm{m}$ was about $-2.0 \pm 2.1\ ^{\circ}\mathrm{C}$, and permafrost extent was about $1.18 \pm 0.02 \times 10^{6}\ \mathrm{km^2\,dec^{-1}}$ over the Tibetan Plateau;

3. The process-based historical simulation revealed steady permafrost degradation over the Tibetan Plateau since 1980. The active layer thickness increased by $0.22\ \mathrm{m}$, permafrost temperature at $15\ \mathrm{m}$ depth increased at a rate of $0.06 \pm 0.01\ ^{\circ}\mathrm{C\,dec^{-1}}$, and permafrost extent degraded by about $10.8\ \%$;

4. Our simulations indicate that current land surface models employing shallow soil columns are inadequate for permafrost research on the Tibetan Plateau, since they have generally underestimated permafrost extent while overestimating degradation rates. Such inadequacy may also pose challenges in other regions characterized by deep active layers (i.e., $> 3\ \mathrm{m}$);

5. This study highlights the ongoing efforts in stand-alone process-based permafrost model development. We hope in the future, with more available stand-alone land-scheme-designed permafrost models, the permafrost community will provide a simulation benchmark for the Earth system model developments as well as the climate change assessment at a global scale.

Appendix A: Latent heat from Priestley-Taylor method

The latent heat flux (Q_e) is treated differently depending on the snow cover, and the FPM uses the Priestley-Taylor method by generally following Martens et al. (2017). If snow is absent, Q_e is the sum of latent heat for bare soil Q_e^s ($W\,m^{-2}$) and covered vegetation Q_e^v ($W\,m^{-2}$).

$$Q_e = Q_e^s + Q_e^v \tag{A1}$$

where Q_e^s and Q_e^v are given as

$$Q_e^s = S_s \alpha_{pt} \frac{\Delta(Q_n^s - Q_c)}{\Delta + \gamma} \tag{A2}$$

$$Q_e^v = S_v \alpha_{pt} \frac{\Delta Q_n^v}{\Delta + \gamma} \tag{A3}$$

where Q_n^s and Q_n^v are the net radiation partitioned for bare soil and vegetation, and derived following Fisher et al. (2008).

$$Q_n^s = f_s Q_n \tag{A4}$$

$$Q_n^v = (1 - f_s) Q_n \tag{A5}$$

where Q_n ($W\,m^{-2}$) is the total net radiation, f_s ($-$) is fractional net radiation reached to the bare soil, and is treated as

$$f_s = \exp(-k_{Rn} LAI) \tag{A6}$$

where k_{Rn} = 0.6 is extinction coefficient from Impens and Lemeur (1969), and LAI ($-$) is Leaf Area Index from MODIS (Table 2).

While α_{pt} is normally set to 1.26 for snow-free areas following the original study (Priestley and Taylor, 1972), many studies reported that it is site-specific, depending on the surface conditions (e.g., Constantin et al., 2015; Martens et al., 2017). In FPM, the parameterization scheme that solves the influences of vegetation and soil moisture on latent heat was used. This is achieved via introducing the evaporation stress factor S ($-$). The S for bare soil (S_s) and vegetation (S_v) are defined as:

$$S_s = 1 - \frac{\theta_c - \theta_R}{\theta_c - \theta_r} \tag{A7}$$

$$S_v = \sqrt{\frac{VOD}{VOD_{max}}} \left(1 - \left(\frac{\theta_c - \theta_R}{\theta_c - \theta_{wp}} \right)^2 \right) \tag{A8}$$

where θ_c ($m^3\,m^{-3}$) is the critical soil moisture, θ_R ($m^3\,m^{-3}$) is the soil moisture in the root zone layer, θ_r ($m^3\,m^{-3}$) is the residual soil moisture, θ_{wp} ($m^3\,m^{-3}$) is soil moisture content of wilting point, VOD ($-$) is vegetation optical depth, and VOD_{max} is the maximum VOD for a given simulation cell. The θ_c is variable depending on the soil texture, and we used the parameters from Zhu et al. (2019). The θ_R ($m^3\,m^{-3}$) is estimated as the ensemble mean of five remote-sensing-based soil moisture (Table 2), θ_{wp} is given in Appendix B, and θ_r is constant of 0.05 $m^3\,m^{-3}$ following Fisher et al. (2008). The VOD is from Moesinger et al. (2020).

If snow is present, the Q_e for a given cell is derived as the weighted mean of the snow and soil cover fractions (SCF), assuming no latent heat via vegetation:

$$Q_e = SCF \cdot Q_e^{sn} + (1 - SCF) \cdot Q_e^s \tag{A9}$$

where Q_e^{sn} is the latent heat from snow-covered area, and is given as

$$Q_e^{sn} = S_{sn}\alpha_{pt}\frac{\Delta(Q_n^{sn} - Q_c)}{\Delta + \gamma} \tag{A10}$$

where S_{sn} and α_{pt} are set to 1 and 0.95, respectively.

Appendix B: Soil organic matter properties

FPM considers the impacts of organic matter on soil hydraulic properties following CoLM (Dai et al., 2003) and SURFEX (Masson et al., 2013):

$$\tau = f_o\tau^o + f_m\tau^m + f_g\tau^g \tag{B1}$$

$$f_o + f_m + f_g = 1 \tag{B2}$$

where f_o ($m^3\,m^{-3}$), f_m ($m^3\,m^{-3}$), and f_g ($m^3\,m^{-3}$) are the fractions of organic matter, mineral and gravel, respectively. The τ refers to the soil hydraulic properties, including: slope of the retention curve b (dimensionless), soil matric potential ψ (dimensionless), soil porosity ϕ ($m^3\,m^{-3}$), field capacity θ_{fc} ($m^3\,m^{-3}$), and wilting point θ_{wp} ($m^3\,m^{-3}$). For gravel, ϕ is set as 0.05 $m^3\,m^{-3}$, and others are set to 0, assuming the soil hydraulic properties are not directly affected by gravel.

The soil organic matter properties τ^o were implicitly accounted for in the FPM:

$$b^o = min\left(2.7 + 9.3 \times \frac{Z_i}{Z_{sap}},\ 12.0\right) \tag{B3}$$

$$\psi_{sat}^o = max\left(10.3 - 0.2 \times \frac{Z_i}{Z_{sap}},\ 10.1\right) \tag{B4}$$

$$\phi^o = max\left(0.93 - 0.1 \times \frac{Z_i}{Z_{sap}},\ 0.83\right) \tag{B5}$$

$$\theta_{fc}^o = min\left(0.37 + 0.35 \times \frac{Z_i}{Z_{sap}},\ 0.72\right) \tag{B6}$$

$$\theta_{wp}^o = min\left(0.07 + 0.15 \times \frac{Z_i}{Z_{sap}},\ 0.22\right) \tag{B7}$$

where Z_i (m) is the soil depth for soil grid of i, and $Z_{sap} = 0.5$ m is the depth that organic matter takes on the characteristics of sapric peat.

The mineral soil hydraulic properties were approximated as:

$$b^m = 2.91 + 15.9 f_{clay} \tag{B8}$$

$$\psi_{sat}^m = -10 \times 10^{(1.88 - 1.31 f_{sand})} \tag{B9}$$

$$\phi^m = 0.489 - 0.126 f_{sand} \tag{B10}$$

$$\theta_{fc}^m = 0.45 \left(f_{clay}\right)^{0.3496} \tag{B11}$$

$$\theta_{wp}^m = 0.37 \sqrt{f_{clay}} \tag{B12}$$

where $\mathrm{f_{clay}}$ ($\mathrm{m^3\,m^{-3}}$) and $\mathrm{f_{sand}}$ ($\mathrm{m^3\,m^{-3}}$) are the volumetric content of clay and sand to the total mineral soil, respectively.

Appendix C: Evaluation metrics

The evaluation metrics of bias (BIAS) and root-mean-square-error (RMSE) were used here to evaluate model performance.

$$BIAS = \frac{1}{N} \sum_{i=1}^{N} (MOD - OBS), \tag{C1}$$

$$RMSE = \sqrt{\frac{1}{N} \sum_{i=1}^{N} (MOD - OBS)^2}, \tag{C2}$$

where OBS and MOD represent the variables of interest (i.e., mean annual ground temperature and active layer thickness) from *in situ* observations and the simulations.

Appendix D: Evaluation of model forcing

The climate forcing was evaluated against *in situ* observations from the synthesis sites (Table 4). Our evaluation results indicate that there is generally a cold bias of the near-surface air temperature ($-1.9\ ^\circ\mathrm{C}$) for the ERA5-Land, and the RMSE was about $3.5\ ^\circ\mathrm{C}$ (Fig. D1). While ERA5-Land slightly overestimated the incoming short-wave radiation (bias = $10.3\ \mathrm{W\,m^{-2}}$), the incoming long-wave radiation was underestimated by about $-24.1\ \mathrm{W\,m^{-2}}$. Overall, the evaluation results indicate that the meteorological variables in the reanalysis dataset are generally consistent with the observations and can be used as suitable forcing/inputs for the numerical simulation.

Appendix E: Nomenclature

In this study, Q ($\mathrm{W\,m^{-2}}$) refers to surface energy balance terms, subscripts identify the term (si: incoming shortwave radiation; li: incoming longwave radiation; le: emitted longwave radiation; h: turbulent exchange of sensible heat; e: turbulent exchange of latent heat; c: energy transport due to conduction; n: net radiation; and m: the energy flux available for melt). We use k ($\mathrm{W\,m^{-1}\,^\circ K^{-1}}$), CV ($\mathrm{J\,m^{-3}\,^\circ K^{-1}}$), and ρ ($\mathrm{kg\,m^{-3}}$) to represent thermal conductivity, volumetric heat capacity, and density,

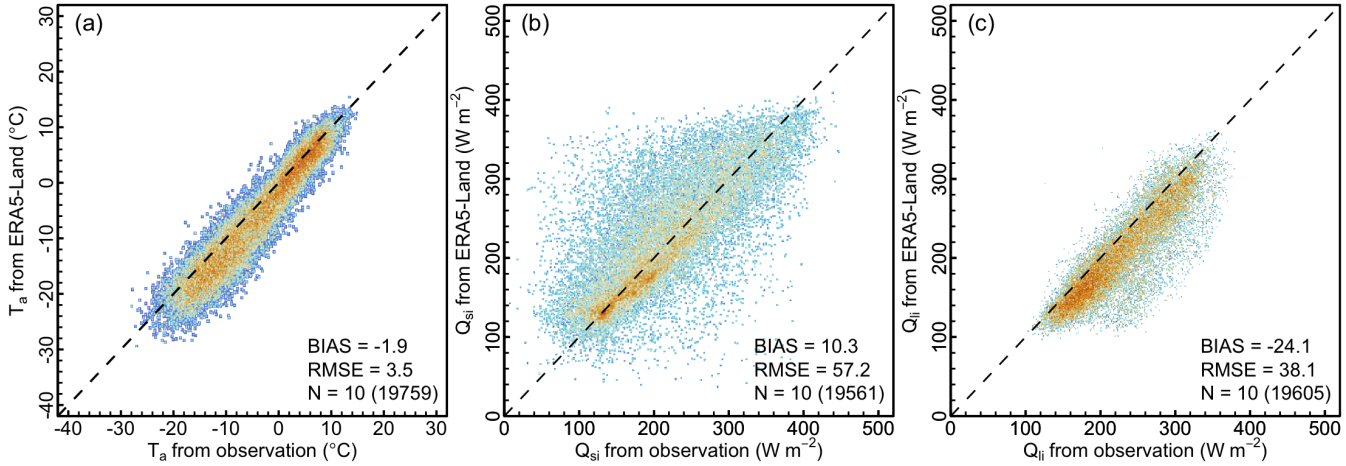

Figure D1. Evaluation of the daily (a) near-surface air temperature (T_a), (b) incoming short-wave radiation (Q_{si}), and (c) incoming long-wave radiation (Q_{li}) from ERA5-Land. The number of meteorological stations (measurements) used for the evaluation are given as N.

Table D1. Ground layer depths (m) and thicknesses (m) for the FPM ground layers configuration.

Depth	Thickness	Layer
0–0.2	0.01	1–20
0.2–1	0.05	21–36
1–5	0.10	37–76
5–10	0.20	77–101
10–20	0.50	102–121
20–50	1.00	122–151
50–150	5.00	151–160

480 respectively. The subscript identifies each source (s: soil; sn: snow; m: mineral; o: organic; w: water; i: ice; a: air; and g: gravel). The volumetric contents for each soil component is represented by f ($\mathrm{m^3\ m^{-3}}$).

Code availability. The Flexible Permafrost Model (FPM) source code is available on request from Bin Cao (bin.cao@itpcas.ac.cn).

Data availability. The active layer thickness, mean annual ground temperature at 15 m depth, and the permafrost extent–as the 45-member ensemble mean–are publicly available via Zenodo (https://10.5281/zenodo.15229474; Sun and Cao, 2025).

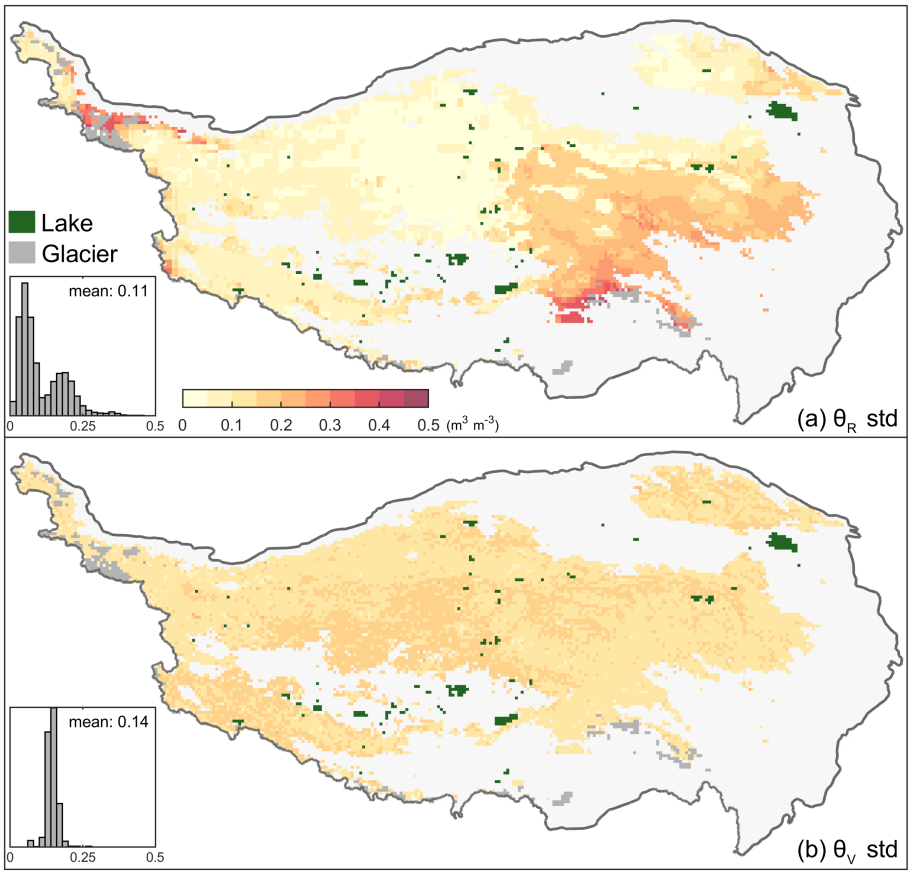

Figure D2. The standard deviation of the soil moisture spread in (a) root (θ_{R}) and (b) vadose (θ_{v}) zones.

Table E1. Nomenclature and input parameters for Flexible Permafrost Model (FPM).

Symbol	Parameter	Value or range	Unit
θ_{wp}	soil moisture content of wilting point		$\mathrm{m^3\,m^{-3}}$
e_a	atmospheric vapor pressure		Pa
σ	Stefan-Boltzmann constant	5.67×10^{-8}	$\mathrm{W\,m^{-2}K^{-4}}$
κ	Von Karman's constant	0.4	Dimensionless
L_f	mass specific latent heat of water	0.334×10^6	$\mathrm{J\,kg^{-1}}$
L_v	latent heat of vaporization	2.471×10^6	$\mathrm{J\,kg^{-1}}$
c_p	specific heat of air	1004.0	$\mathrm{J\,K^{-1}\,kg^{-1}}$

Author contributions. WS carried out this study by developing model, analyzing data, performing the simulations, and writing the paper and was responsible for the compilation and quality control of the observations. BC conceived and guided the project, proposed the initial idea,

designed model structure as well as parameterizations, developed and tested the model, and contributed to organizing as well as writing the paper.

Competing interests. The authors declare that they have no conflict of interest.

Acknowledgements. The authors thank Kun Zhang for his helpful suggestions in model development and Shengdi Wang for developing and testing the early version of model. ERA5-Land reanalysis data and the ESA CCI LC map are provided by the ECMWF.

This study was supported by the National Natural Science Foundation of China (grant no. 42422608), the Youth Innovation Promotion Association Chinese Academy of Sciences (grant no. 2023075) to B. Cao. W. Sun was supported by the China Postdoctoral Science Foundation (grant no. 2023M733604).

References

Agam, N., Kustas, W. P., Anderson, M. C., Norman, J. M., Colaizzi, P. D., Howell, T. A., Prueger, J. H., Meyers, T. P., and Wilson, T. B.: Application of the Priestley–Taylor Approach in a Two-Source Surface Energy Balance Model, Journal of Hydrometeorology, 11, 185–198, https://doi.org/10.1175/2009JHM1124.1, 2010.

Biskaborn, B. K., Lanckman, J.-P., Lantuit, H., Elger, K., Streletskiy, D., Cable, W., and Romanovsky, V. E.: The new database of the Global Terrestrial Network for Permafrost (GTN-P), Earth System Science Data, 7, 245–259, https://doi.org/10.5194/essd-7-245-2015, 2015.

Biskaborn, B. K., Smith, S. L., Noetzli, J., Matthes, H., Vieira, G., Streletskiy, D. A., Schoeneich, P., Romanovsky, V. E., Lewkowicz, A. G., and Abramov, A.: Permafrost is warming at a global scale, Nature communications, 10, 1–11, https://doi.org/10.1038/s41467-018-08240-4, 2019.

Brunt, D.: Physical and dynamical meteorology, Cambridge University Press, 2011.

Burke, E. J., Zhang, Y., and Krinner, G.: Evaluating Permafrost Physics in the Coupled Model Intercomparison Project 6 (CMIP6) Models and Their Sensitivity to Climate Change, The Cryosphere, 14, 3155–3174, https://doi.org/10.5194/tc-14-3155-2020, 2020.

Cao, B. and Gruber, S.: Brief communication: Reanalyses underperform in cold regions, raising concerns for climate services and research, The Cryosphere, 19, 4525–4532, https://doi.org/10.5194/tc-19-4525-2025, 2025.

Cao, B., Gruber, S., and Zhang, T.: REDCAPP (v1. 0): Parameterizing valley inversions in air temperature data downscaled from reanalyses, Geoscientific Model Development, 10, 2905–2923, https://doi.org/10.5194/gmd-10-2905-2017, 2017a.

Cao, B., Gruber, S., Zhang, T., Li, L., Peng, X., Wang, K., Zheng, L., Shao, W., and Guo, H.: Spatial variability of active layer thickness detected by ground-penetrating radar in the Qilian Mountains, Western China, Journal of Geophysical Research: Earth Surface, 122, 574–591, https://doi.org/10.1002/2016JF004018, 2017b.

Cao, B., Zhang, T., Peng, X., Mu, C., Wang, Q., Zheng, L., Wang, K., and Zhong, X.: Thermal characteristics and recent changes of permafrost in the upper reaches of the heihe river basin, Western China, Journal of Geophysical Research: Atmospheres, 123, 7935–7949, https://doi.org/10.1029/2018JD028442, 2018.

Cao, B., Quan, X., Brown, N., Stewart-Jones, E., and Gruber, S.: GlobSim (v1. 0): deriving meteorological time series for point locations from multiple global reanalyses, Geoscientific Model Development, 12, 4661–4679, https://doi.org/10.5194/gmd-12-4661-2019, 2019a.

Cao, B., Zhang, T., Wu, Q., Sheng, Y., Zhao, L., and Zou, D.: Permafrost zonation index map and statistics over the Qinghai–Tibet Plateau based on field evidence, Permafrost Periglacial Processes, 30, 178–194, https://doi.org/10.1002/ppp.2006, 2019b.

Cao, B., Li, X., Feng, M., and Zheng, D.: Quantifying overestimated permafrost extent driven by rock glacier inventory, Geophysical Research Letters, 48, e2021GL092 476, https://doi.org/10.1029/2021GL092476, 2021.

Cao, B., Arduini, G., and Zsoter, E.: Brief communication: Improving ERA5-Land soil temperature in permafrost regions using an optimized multi-layer snow scheme, The Cryosphere, 16, 2701–2708, https://doi.org/10.5194/tc-16-2701-2022, 2022.

Chadburn, S., Burke, E., Essery, R., Boike, J., Langer, M., Heikenfeld, M., Cox, P. M., and Friedlingstein, P.: Impact of model developments on present and future simulations of permafrost in a global land-surface model, The Cryosphere, 9, 1505–1521, https://doi.org/10.5194/tc-9-1505-2015, 2015.

Chadburn, S., Burke, E., Cox, P., Friedlingstein, P., Hugelius, G., and Westermann, S.: An observation-based constraint on permafrost loss as a function of global warming, Nature Climate Change, 7, 340–344, https://doi.org/10.1038/nclimate3262, 2017.

Chen, R., Nitzbon, J., von Deimling, T. S., Stuenzi, S. M., Chan, N.-H., Boike, J., and Langer, M.: Potential vegetation greenness changes in the permafrost areas over the Tibetan Plateau under future climate warming, Global and Planetary Change, p. 104833, https://doi.org/https://doi.org/10.1016/j.gloplacha.2025.104833, 2025.

Chen, Y., Lara, M. J., Jones, B. M., Frost, G. V., and Hu, F. S.: Thermokarst Acceleration in Arctic Tundra Driven by Climate Change and Fire Disturbance, One Earth, 4, 1718–1729, https://doi.org/10.1016/j.oneear.2021.11.011, 2021.

Constantin, J., Willaume, M., Murgue, C., Lacroix, B., and Therond, O.: The soil-crop models STICS and AqYield predict yield and soil water content for irrigated crops equally well with limited data, Agricultural and Forest Meteorology, 206, 55–68, https://doi.org/10.1016/j.agrformet.2015.02.011, 2015.

Cosenza, P., Guérin, R., and Tabbagh, A.: Relationship between thermal conductivity and water content of soils using numerical modelling, European Journal of Soil Science, 54, 581–588, https://doi.org/10.1046/j.1365-2389.2003.00539.x, 2003.

Dai, Y., Zeng, X., Dickinson, R. E., Baker, I., Bonan, G. B., Bosilovich, M. G., Denning, A. S., Dirmeyer, P. A., Houser, P. R., Niu, G., et al.: The common land model, Bulletin of the American Meteorological Society, 84, 1013–1024, https://doi.org/10.1175/BAMS-84-8-1013, 2003.

Dai, Y., Xin, Q., Wei, N., Zhang, Y., Shangguan, W., Yuan, H., Zhang, S., Liu, S., and Lu, X.: A Global High-Resolution Data Set of Soil Hydraulic and Thermal Properties for Land Surface Modeling, Journal of Advances in Modeling Earth Systems, 11, 2996–3023, https://doi.org/10.1029/2019MS001784, 2019.

Davies, J. H.: Global map of solid Earth surface heat flow, Geochemistry, Geophysics, Geosystems, 14, 4608–4622, https://doi.org/10.1002/ggge.20271, 2013.

Decharme, B., Douville, H., Boone, A., Habets, F., and Noilhan, J.: Impact of an exponential profile of saturated hydraulic conductivity within the ISBA LSM: simulations over the Rhône basin, Journal of Hydrometeorology, 7, 61–80, https://doi.org/10.1175/JHM469.1, 2006.

Devoie, É. G., Craig, J. R., Connon, R. F., and Quinton, W. L.: Taliks: A Tipping Point in Discontinuous Permafrost Degradation in Peatlands, Water Resources Research, 55, 9838–9857, https://doi.org/10.1029/2018WR024488, 2019.

Dingman, S. L.: Physical hydrology, Waveland press, 2015.

Dorigo, W., Wagner, W., Albergel, C., Albrecht, F., Balsamo, G., Brocca, L., Chung, D., Ertl, M., Forkel, M., Gruber, A., et al.: ESA CCI Soil Moisture for improved Earth system understanding: State-of-the art and future directions, Remote Sensing of Environment, 203, 185–215, https://doi.org/10.1016/j.rse.2017.07.001, 2017.

Douville, H., Royer, J. F., and Mahfouf, J. F.: A new snow parameterization for the Météo-France climate model: Part I: validation in stand-alone experiments, Climate Dynamics, 12, 21–35, https://doi.org/10.1007/BF00208760, 1995.

Endrizzi, S., Gruber, S., Dall'Amico, M., and Rigon, R.: GEOtop 2.0: simulating the combined energy and water balance at and below the land surface accounting for soil freezing, snow cover and terrain effects, Geoscientific Model Development, 7, 2831–2857, https://doi.org/10.5194/gmd-7-2831-2014, 2014.

Fan, Y., Li, H., and Miguez-Macho, G.: Global patterns of groundwater table depth, Science, 339, 940–943, https://doi.org/10.1126/science.1229881, 2013.

Fernandez-Moran, R., Al-Yaari, A., Mialon, A., Mahmoodi, A., Al Bitar, A., De Lannoy, G., Rodriguez-Fernandez, N., Lopez-Baeza, E., Kerr, Y., and Wigneron, J.-P.: SMOS-IC: An alternative SMOS soil moisture and vegetation optical depth product, Remote Sensing, 9, 457, https://doi.org/10.3390/rs9050457, 2017.

Fiddes, J. and Gruber, S.: TopoSCALE v.1.0: downscaling gridded climate data in complex terrain, Geoscientific Model Development, 7, 387–405, https://doi.org/10.5194/gmd-7-387-2014, 2014.

Fiddes, J., Endrizzi, S., and Gruber, S.: Large-Area Land Surface Simulations in Heterogeneous Terrain Driven by Global Data Sets: Application to Mountain Permafrost, The Cryosphere, 9, 411–426, https://doi.org/10.5194/tc-9-411-2015, 2015.

Fisher, J. B., Tu, K. P., and Baldocchi, D. D.: Global estimates of the land–atmosphere water flux based on monthly AVHRR and ISLSCP-II data, validated at 16 FLUXNET sites, Remote Sensing of Environment, 112, 901–919, https://doi.org/10.1016/j.rse.2007.06.025, 2008.

Fleagle, R. G. and Businger, J. A.: An introduction to atmospheric physics, Academic Press, 1981.

Gao, B., Yang, D., Qin, Y., Wang, Y., Li, H., Zhang, Y., and Zhang, T.: Change in frozen soils and its effect on regional hydrology, upper Heihe basin, northeastern Qinghai-Tibetan Plateau, The Cryosphere, 12, https://doi.org/10.5194/tc-2016-289, 2018.

Gao, H., Han, C., Chen, R., Feng, Z., Wang, K., Fenicia, F., and Savenije, H.: Frozen Soil Hydrological Modeling for a Mountainous Catchment Northeast of the Qinghai–Tibet Plateau, Hydrology and Earth System Sciences, 26, 4187–4208, https://doi.org/10.5194/hess-26-4187-2022, 2022.

Göckede, M., Kittler, F., Kwon, M. J., Burjack, I., Heimann, M., Kolle, O., Zimov, N., and Zimov, S.: Shifted energy fluxes, increased Bowen ratios, and reduced thaw depths linked with drainage-induced changes in permafrost ecosystem structure, The Cryosphere, 11, 2975–2996, https://doi.org/10.5194/tc-11-2975-2017, 2017.

Gruber, S.: Derivation and analysis of a high-resolution estimate of global permafrost zonation, The Cryosphere, 6, 221–233, https://doi.org/10.5194/tc-6-221-2012, 2012.

Gubler, S., Endrizzi, S., Gruber, S., and Purves, R. S.: Sensitivities and uncertainties of modeled ground temperatures in mountain environments, Geoscientific Model Development, 6, 1319–1336, https://doi.org/10.5194/gmd-6-1319-2013, 2013.

Guo, D. and Wang, H.: Simulation of permafrost and seasonally frozen ground conditions on the Tibetan Plateau, 1981–2010, Journal of Geophysical Research: Atmospheres, 118, 5216–5230, https://doi.org/10.1002/jgrd.50457, 2013.

Guo, D., Wang, A., Li, D., and Hua, W.: Simulation of changes in the near-surface soil freeze/thaw cycle using clm4. 5 with four atmospheric forcing data sets, Journal of Geophysical Research: Atmospheres, 123, 2509–2523, https://doi.org/10.1002/2017JD028097, 2018.

Hjort, J., Karjalainen, O., Aalto, J., Westermann, S., Romanovsky, V. E., Nelson, F. E., Etzelmüller, B., and Luoto, M.: Degrading permafrost puts Arctic infrastructure at risk by mid-century, Nature communications, 9, 1–9, https://doi.org/10.1038/s41467-018-07557-4, 2018.

Hock, R., Rasul, G., Adler, C., Cáceres, B., Gruber, S., Hirabayashi, Y., Jackson, M., Kääb, A., Kang, S., Kutuzov, S., et al.: High mountain areas. IPCC special report on the ocean and cryosphere in a changing climate. H.-O. Pörtner, DC Roberts, V, 2019.

Hou, X.: 1:1 million vegetation map of China, A Big Earth Data Platform for Three Poles, http://dx.doi.org, 2019.

Impens, I. and Lemeur, R.: Extinction of Net Radiation in Different Crop Canopies, Archiv für Meteorologie, Geophysik und Bioklimatologie Serie B, 17, 403–412, https://doi.org/10.1007/BF02243377, 1969.

Jafarov, E. E., Marchenko, S. S., and Romanovsky, V. E.: Numerical modeling of permafrost dynamics in Alaska using a high spatial resolution dataset, The Cryosphere, 6, 613–624, https://doi.org/10.5194/tc-6-613-2012, 2012.

Jan, A., Coon, E. T., and Painter, S. L.: Evaluating integrated surface/subsurface permafrost thermal hydrology models in ATS (v0.88) against observations from a polygonal tundra site, Geoscientific Model Development, 13, 2259–2276, https://doi.org/10.5194/gmd-13-2259-2020, 2020.

Jia, A., Wang, D., Liang, S., Peng, J., and Yu, Y.: Global daily actual and snow-free blue-sky land surface albedo climatology from 20-year MODIS products, Journal of Geophysical Research: Atmospheres, 127, e2021JD035 987, https://doi.org/10.1029/2021JD035987, 2022.

Langer, M., Nitzbon, J., Groenke, B., Assmann, L.-M., Schneider von Deimling, T., Stuenzi, S. M., and Westermann, S.: The evolution of Arctic permafrost over the last 3 centuries from ensemble simulations with the CryoGridLite permafrost model, The Cryosphere, 18, 363–385, https://doi.org/doi.org/10.5194/tc-18-363-202, 2024.

Ling, F. and Zhang, T.: A numerical model for surface energy balance and thermal regime of the active layer and permafrost containing unfrozen water, Cold Regions Science Technology, 38, 1–15, https://doi.org/10.1016/S0165-232X(03)00057-0, 2004.

Linmao, G., Genxu, W., Chunlin, S., Shouqin, S., Kai, L., Jinlong, L., Yang, L., Biying, Z., Jiapei, M., and Peng, H.: Development of a Modular Distributed Hydro-Thermal Coupled Hydrological Model for Cold Regions, Journal of Hydrology, 644, 132 099, https://doi.org/10.1016/j.jhydrol.2024.132099, 2024.

Liston, G. E. and Hall, D. K.: An energy-balance model of lake-ice evolution, Journal of Glaciology, 41, 373–382, https://doi.org/10.3189/S0022143000016245, 1995.

Martens, B., Miralles, D. G., Lievens, H., van der Schalie, R., De Jeu, R. A. M., Fernández-Prieto, D., Beck, H. E., Dorigo, W. A., and Verhoest, N. E. C.: GLEAM v3: satellite-based land evaporation and root-zone soil moisture, Geoscientific Model Development, 10, 1903–1925, https://doi.org/10.5194/gmd-10-1903-2017, 2017.

Masson, V., Le Moigne, P., Martin, E., Faroux, S., Alias, A., Alkama, R., Belamari, S., Barbu, A., Boone, A., Bouyssel, F., et al.: The SURFEXv7. 2 land and ocean surface platform for coupled or offline simulation of earth surface variables and fluxes, Geoscientific Model Development, 6, 929–960, https://doi.org/10.5194/gmd-6-929-2013, 2013.

McKenzie, J. M., Voss, C. I., and Siegel, D. I.: Groundwater flow with energy transport and water–ice phase change: Numerical simulations, benchmarks, and application to freezing in peat bogs, Advances in Water Resources, 30, 966–983, https://doi.org/10.1016/j.advwatres.2006.08.008, 2007.

Moesinger, L., Dorigo, W., de Jeu, R., van der Schalie, R., Scanlon, T., Teubner, I., and Forkel, M.: The global long-term microwave vegetation optical depth climate archive (VODCA), Earth System Science Data, 12, 177–196, https://doi.org/10.5194/essd-12-177-2020, 2020.

Muñoz-Sabater, J., Dutra, E., Agustí-Panareda, A., Albergel, C., Arduini, G., Balsamo, G., Boussetta, S., Choulga, M., Harrigan, S., Hersbach, H., et al.: ERA5-Land: A state-of-the-art global reanalysis dataset for land applications, Earth system science data, 13, 4349–4383, https://doi.org/10.5194/essd-13-4349-2021, 2021.

Myneni, R., Knyazikhin, Y., and Park, T.: MODIS/Terra Leaf Area Index/FPAR 8-Day L4 Global 500m SIN Grid V061 [Data set], NASA EOSDIS Land Processes Distributed Active Archive Center, 2021.

Nicolsky, D., Romanovsky, V., Alexeev, V., and Lawrence, D.: Improved modeling of permafrost dynamics in a GCM land-surface scheme, Geophysical Research Letters, 34, https://doi.org/10.1029/2007GL029525, 2007.

Niu, G.-Y. and Yang, Z.-L.: Effects of frozen soil on snowmelt runoff and soil water storage at a continental scale, Journal of Hydrometeorology, 7, 937–952, https://doi.org/10.1175/JHM538.1, 2006.

Obu, J., Westermann, S., Bartsch, A., Berdnikov, N., Christiansen, H. H., Dashtseren, A., Delaloye, R., Elberling, B., Etzelmüller, B., and Kholodov, A.: Northern Hemisphere permafrost map based on TTOP modelling for 2000–2016 at 1 km2 scale, Earth-Science Reviews, 193, 299–316, https://doi.org/10.1016/j.earscirev.2019.04.023, 2019.

Orsolini, Y., Wegmann, M., Dutra, E., Liu, B., Balsamo, G., Yang, K., de Rosnay, P., Zhu, C., Wang, W., Senan, R., et al.: Evaluation of snow depth and snow cover over the Tibetan Plateau in global reanalyses using in situ and satellite remote sensing observations, The Cryosphere, 13, 2221–2239, https://doi.org/10.5194/tc-13-2221-2019, 2019.

O'Neill, P., Chan, S., Njoku, E., Jackson, T., Bindlish, R., and Chaubell, J.: L3 Radiometer Global Daily 36 km EASE-Grid Soil Moisture [data set], https://doi.org/10.5067/4XXOGX0OOW1S, 2021.

Pan, X., Li, Y., Yu, Q., Shi, X., Yang, D., and Roth, K.: Effects of Stratified Active Layers on High-Altitude Permafrost Warming:A Case Study on the Qinghai–Tibet Plateau, The Cryosphere, 10, 1591–1603, https://doi.org/10.5194/tc-10-1591-2016, 2016.

Parinussa, R. M., Holmes, T. R., Wanders, N., Dorigo, W. A., and de Jeu, R. A.: A preliminary study toward consistent soil moisture from AMSR2, Journal of Hydrometeorology, 16, 932–947, https://doi.org/10.1175/JHM-D-13-0200.1, 2015.

Price, A. and Dunne, T.: Energy balance computations of snowmelt in a subarctic area, Water Resources Research, 12, 686–694, https://doi.org/10.1029/WR012i004p00686, 1976.

Priestley, C. H. B. and Taylor, R. J.: On the assessment of surface heat flux and evaporation using large-scale parameters, Monthly Weather Review, 100, 81–92, https://doi.org/10.1175/1520-0493(1972)100<0081:OTAOSH>2.3.CO;2, 1972.

Qin, Y., Wu, T., Zhao, L., Wu, X., Li, R., Xie, C., Pang, Q., Hu, G., Qiao, Y., Zhao, G., et al.: Numerical modeling of the active layer thickness and permafrost thermal state across Qinghai-Tibetan Plateau, Journal of Geophysical Research: Atmospheres, 122, 11–604, https://doi.org/10.1002/2017JD026858, 2017.

SAF, H.: ASCAT Surface Soil Moisture Climate Data Record v5 12.5 km sampling–Metop, EUMETSAT SAF on Support to Operational Hydrology and Water Management [data set], https://doi.org/10.15770/EUM_SAF_H_0009, 2020.

Schuur, E. A. and Mack, M. C.: Ecological response to permafrost thaw and consequences for local and global ecosystem services, Annual Review of Ecology, Evolution, Systematics, 49, 279–301, https://doi.org/10.1146/annurev-ecolsys-121415-032349, 2018.

Schuur, E. A., McGuire, A. D., Schädel, C., Grosse, G., Harden, J., Hayes, D. J., Hugelius, G., Koven, C. D., Kuhry, P., and Lawrence, D. M.: Climate change and the permafrost carbon feedback, Nature, 520, 171–179, https://doi.org/10.1038/nature14338, 2015.

Schädel, C., Rogers, B. M., Lawrence, D. M., Koven, C. D., Brovkin, V., Burke, E. J., Genet, H., Huntzinger, D. N., Jafarov, E., McGuire, A. D., Riley, W. J., and Natali, S. M.: Earth system models must include permafrost carbon processes, Nature Climate Change, 14, 114–116, https://doi.org/10.1038/s41558-023-01909-9, 2024.

Shangguan, W., Hengl, T., Mendes de Jesus, J., Yuan, H., and Dai, Y.: Mapping the global depth to bedrock for land surface modeling, Journal of Advances in Modeling Earth Systems, 9, 65–88, https://doi.org/10.1002/2016ms000686, 2017.

Song, L., Kustas, W. P., Liu, S., Colaizzi, P. D., Nieto, H., Xu, Z., Ma, Y., Li, M., Xu, T., Agam, N., Tolk, J. A., and Evett, S. R.: Applications of a thermal-based two-source energy balance model using Priestley-Taylor approach for surface temperature partitioning under advective conditions, Journal of Hydrology, 540, 574–587, https://doi.org/10.1016/j.jhydrol.2016.06.034, 2016.

Song, L., Wang, L., Li, X., Zhou, J., Luo, D., Jin, H., Qi, J., Zeng, T., and Yin, Y.: Improving Permafrost Physics in a Distributed Cryosphere-Hydrology Model and Its Evaluations at the Upper Yellow River Basin, Journal of Geophysical Research: Atmospheres, 125, e2020JD032 916, https://doi.org/10.1029/2020JD032916, 2020.

Sun, W. and Cao, B.: Ensemble numerical simulation of permafrost over the Tibetan Plateau from Flexible Permafrost Model:1950–2023 [data set], https://doi.org/10.5281/zenodo.15229474, 2025.

Sun, W., Zhang, T., Clow, G. D., Sun, Y., Zhao, W., Liang, B., Fan, C., Peng, X., and Cao, B.: Observed permafrost thawing and disappearance near the altitudinal limit of permafrost in the Qilian Mountains, Advances in Climate Change Research, https://doi.org/10.1016/j.accre.2022.08.004, 2022.

Sun, W., Cao, B., Hao, J., Wang, S., Clow, G. D., Sun, Y., Fan, C., Zhao, W., Peng, X., Yao, Y., et al.: Two-dimensional simulation of island permafrost degradation in Northeastern Tibetan Plateau, Geoderma, 430, 116 330, https://doi.org/10.1016/j.geoderma.2023.116330, 2023.

Tubini, N., Gruber, S., and Rigon, R.: A method for solving heat transfer with phase change in ice or soil that allows for large time steps while guaranteeing energy conservation, The Cryosphere, 15, 2541–2568, https://doi.org/10.5194/tc-15-2541-2021, 2021.

Verseghy, D. L.: Class—A Canadian land surface scheme for GCMS. I. Soil model, International Journal of Climatology, 11, 111–133, https://doi.org/10.1002/joc.3370110202, 1991.

Walvoord, M. A., Voss, C. I., Ebel, B. A., and Minsley, B. J.: Development of perennial thaw zones in boreal hillslopes enhances potential mobilization of permafrost carbon, Environmental Research Letters, 14, 015 003, https://doi.org/10.1088/1748-9326/aaf0cc, 2019.

Wellman, T. P., Voss, C. I., and Walvoord, M. A.: Impacts of Climate, Lake Size, and Supra- and Sub-Permafrost Groundwater Flow on Lake-Talik Evolution, Yukon Flats, Alaska (USA), Hydrogeology Journal, 21, 281–298, https://doi.org/10.1007/s10040-012-0941-4, 2013.

Westermann, S., Langer, M., Boike, J., Heikenfeld, M., Peter, M., Etzelmüller, B., and Krinner, G.: Simulating the thermal regime and thaw processes of ice-rich permafrost ground with the land-surface model CryoGrid 3, Geoscientific Model Development, 9, 523–546, https://doi.org/10.5194/gmd-9-523-2016, 2016.

Westermann, S., Ingeman-Nielsen, T., Scheer, J., Aalstad, K., Aga, J., Chaudhary, N., Etzelmüller, B., Filhol, S., Kääb, A., Renette, C., Schmidt, L. S., Schuler, T. V., Zweigel, R. B., Martin, L., Morard, S., Ben-Asher, M., Angelopoulos, M., Boike, J., Groenke, B., Miesner, F., Nitzbon, J., Overduin, P., Stuenzi, S. M., and Langer, M.: The CryoGrid community model (version 1.0) – a multi-physics toolbox for climate-driven simulations in the terrestrial cryosphere, Geoscientific Model Development, 16, 2607–2647, https://doi.org/10.5194/gmd-16-2607-2023, 2023.

Wu, X., Nan, Z., Zhao, S., Zhao, L., Cheng, G. J. P., and Processes, P.: Spatial modeling of permafrost distribution and properties on the Qinghai-Tibet Plateau, Permafrost Periglacial Processes, 29, 86–99, https://doi.org/10.1002/ppp.1971, 2018.

Zhang, G., Nan, Z., Yin, Z., and Zhao, L.: Isolating the Contributions of Seasonal Climate Warming to Permafrost Thermal Responses Over the Qinghai-Tibet Plateau, JGR Atmospheres, 126, e2021JD035 218, https://doi.org/10.1029/2021JD035218, 2021.

Zhang, T.: Influence of the seasonal snow cover on the ground thermal regime: An overview, Reviews of Geophysics, 43, https://doi.org/10.1029/2004RG000157, 2005.

Zhang, Y., Cheng, G., Li, X., Jin, H., Yang, D., Flerchinger, G. N., Chang, X., Bense, V. F., Han, X., and Liang, J.: Influences of Frozen Ground and Climate Change on Hydrological Processes in an Alpine Watershed: A Case Study in the Upstream Area of the Hei'he River, Northwest China: Influences of Frozen Soil Dynamics on Hydrological Processes, Permafrost and Periglacial Processes, 28, 420–432, https://doi.org/10.1002/ppp.1928, 2017.

Zhao, L., Zou, D., Hu, G., Wu, T., Du, E., Liu, G., Xiao, Y., Li, R., Pang, Q., and Qiao, Y.: A synthesis dataset of permafrost thermal state for the Qinghai–Tibet (Xizang) Plateau, China, Earth System Science Data, 13, 4207–4218, https://doi.org/10.5194/essd-13-4207-2021, 2021.

Zheng, G., Yang, Y., Yang, D., Dafflon, B., Yi, Y., Zhang, S., Chen, D., Gao, B., Wang, T., Shi, R., and Wu, Q.: Remote Sensing Spatiotemporal Patterns of Frozen Soil and the Environmental Controls over the Tibetan Plateau during 2002–2016, Remote Sensing of Environment, 247, 111 927, https://doi.org/10.1016/j.rse.2020.111927, 2020.

Zhu, G., Zhang, K., Chen, H., Wang, Y., Su, Y., Zhang, Y., and Ma, J.: Development and evaluation of a simple hydrologically based model for terrestrial evapotranspiration simulations, Journal of Hydrology, 577, 123 928, https://doi.org/10.1016/j.jhydrol.2019.123928, 2019.

Zou, D., Zhao, L., Yu, S., Chen, J., Hu, G., Wu, T., Wu, J., Xie, C., Wu, X., and Pang, Q.: A new map of permafrost distribution on the Tibetan Plateau, The Cryosphere, 11, 2527, https://doi.org/10.5194/tc-11-2527-2017, 2017.

Zwieback, S., Westermann, S., Langer, M., Boike, J., Marsh, P., and Berg, A.: Improving Permafrost Modeling by Assimilating Remotely Sensed Soil Moisture, Water Resources Research, 55, 1814–1832, https://doi.org/10.1029/2018wr023247, 2019.